International Journal of Solids and Structures 193–194 (2020) 152–171

Contents lists available at ScienceDirect

International Journal of Solids and Structures

journal homepage: www.elsevier.com/locate/ijsolstr

Optimized bi-material layouts for energy dissipating composites under finite deformations

Ryan Alberdi[a], Kapil Khandelwal[b,*]

[a] Dept. of Civil & Env. Engg. & Earth Sci., University of Notre Dame, United States
[b] Dept. of Civil & Env. Engg. & Earth Sci., 156 Fitzpatrick Hall, University of Notre Dame, Notre Dame, IN 46556, United States

ARTICLE INFO

Article history:
Received 17 December 2018
Revised 25 November 2019
Accepted 3 February 2020
Available online 5 February 2020

Keywords:
Architected bi-material composites
Nonlinear topology optimization
RVE-based multiscale models
Computational homogenization
Finite deformation viscoplasticity

ABSTRACT

This study investigates the use of topology optimization as a method for discovering novel layouts of material phases which enhance the energy dissipation capacity of bi-material polymeric composites. Motivated by the experimental and numerical results in Wang et al. (2011), a multi-material topology optimization approach is developed to design composites consisting of a hard glassy polymer phase and soft elastomer phase undergoing large deformations. Computational homogenization is carried out to simulate the composite behavior and the energy dissipated as plastic work in the glassy polymer phase is maximized. The topology optimization examples investigated herein show the ability of the developed framework to exploit the physical phenomena reported in Wang et al. (2011) to improve energy dissipation capacity. Different deformation modes are considered and the influence of symmetry, phase volume fraction, and material rate effects on optimized composites is investigated. Additionally, the design of composites with a soft phase providing energy dissipation capacity and hard phase providing stiffness is carried out to show how vastly different phenomena are exploited to dissipate energy in optimized composites of this type.

1. Introduction

In natural materials, hard and soft phases are commonly used in conjunction to enhance mechanical properties such as stiffness, toughness and energy dissipation (Barthelat, 2015; Zhao et al., 2014). A number of recent studies aimed at improving the performance of engineered composites have used this observation as a guiding principle, focusing on the use of polymeric materials for both the hard and soft composite phases. The use of polymeric materials is motivated by their numerous advantageous properties, which include low cost, light weight, durability, scalability, and multi-functionality (Landel and Nielsen, 1993; Mai and Yu, 2006). Moreover, there has been profusion of additive manufacturing technologies in recent years which can employ and combine a vast range of polymeric materials with different mechanical properties and functionalities, allowing for freeform design of advanced multifunctional polymeric composites (Khoo et al., 2015; Vaezi et al., 2013).

The use of additively manufactured polymeric materials to design bi-material periodic composites consisting of hard glassy polymer and soft elastomer phases was investigated numerically and experimentally in Wang et al. (2011). These composites were designed based on level set structures associated with triply periodic minimal surfaces with varying volume fractions of the hard and soft phases. It was found that the inclusion of the soft elastomeric phase constrains and provides support to the hard glassy phase, redistributing stresses throughout the composite so that a more uniform stress distribution can occur in the hard glassy phase. The result is that the bi-material composites have more even stress distributions and enhanced stiffness compared to corresponding cellular materials using only the glassy polymer phase. Moreover, plastic yielding in the hard glassy phase was found to occur for a greater volume of material when supported by the soft elastomeric material, resulting in enhanced energy dissipation capacity. These findings suggest that such phenomena can be exploited so as to improve the energy dissipation capacity of composites by spreading plastic deformation throughout the energy dissipating glassy phase, prompting the consideration of these types of composites for use as energy dissipative elements in advanced structural components and armors (David et al., 2009; Hogg, 2006).

A number of studies have been carried out to further investigate the properties of these bi-material polymeric composites, with the stress transfer and strain sharing mechanisms reported in Wang et al. (2011) also observed experimentally in Al-Ketan et al. (2017) and Sabet et al. (2018). The influence of

---

[*] Corresponding author.
E-mail address: kapil.khandelwal@nd.edu (K. Khandelwal).

https://doi.org/10.1016/j.ijsolstr.2020.02.006
0020-7683/© 2020 Elsevier Ltd. All rights reserved.

connectivity on the composite performance was investigated in Cho et al. (2016) and Sabet et al. (2018), and it was shown that use of a continuous hard phase results in enhanced stiffness compared to disperse composites such as particle-reinforced, fiber-reinforced and lamellar types. Additionally, the anisotropy of the connected composites was found to be higher than that of disperse composites at low volume fractions, but the opposite trend was observed at higher volume fractions (Cho et al., 2016). These types of composites have also been investigated for use in acoustic bandgap enhancement (Chen and Wang, 2014), where it was shown that they can lead to a coupling of local resonance and Bragg scattering phenomena by tailoring the topological arrangements of the phases. All of these studies show the promise of bi-material composites for enhancing properties such as stiffness, toughness and energy dissipation. Moreover, they have emphasized how the topological arrangement and volume fraction of constituent phases plays a large role in the composite performance and how the use of additive manufacturing techniques provides a high degree of control over the layout of constituent phases even at small scales. Hence, a computational design methodology such as topology optimization (Bendsøe and Sigmund, 2003) – which provides precise control over the topological arrangement of material phases – is a natural fit for use in discovering novel material layouts for performance-optimized composites with enhanced properties such as energy dissipation capacity.

The use of topology optimization to discover composite material designs can be traced back to the early works by Swan and Kosaka (1997) and Swan and Arora (1997), where hybrid Voigt-Reuss mixing rules were used to obtain composites optimized for homogenized properties such as stiffness (Swan and Kosaka, 1997) and a combination of stiffness and ultimate strength (Swan and Arora, 1997). Notably, in Swan and Arora (1997) elastoplastic composites consisting of a hard Boron phase and soft epoxy phase are optimized for ultimate strength, which is closely related to energy dissipation capacity. The optimized composite design obtained therein has a well-connected hard phase and shows a significant improvement in terms of ultimate strength compared to a disperse aligned fiber composite. Subsequent studies have been mostly limited in their focus to the design of composites for improved stiffness properties. For example, in Gibiansky and Sigmund (2000) and (Sigmund, 2000) topology optimization was applied to obtain optimized elastic composites with extreme bulk modulus values approaching theoretical bounds. In de Souza Neto et al. (2010) and Amstutz et al. (2010), a level set approach based on the topological derivative was used to design composites by maximizing bulk and shear moduli as well as maximizing and minimizing Poisson's ratios. Stiffness properties of viscoelastic composites have also been improved by using topology optimization; e.g. by optimizing homogenized loss and storage moduli (Andreasen et al., 2014; Chen and Liu, 2014; Yi et al., 2000; Yun and Youn, 2018), or maximizing acoustic loss factor in target frequency ranges when the composite behavior of viscoelastic material and air are considered (Kook and Jensen, 2017). Interestingly, in Andreasen et al. (2014) the resulting optimized composites were able to achieve the theoretical upper bound for bulk loss modulus if the hard phase was unconnected, but constraining the hard phase to be connected resulted in bulk loss moduli unable to reach the upper bound. Additionally, topology optimization of electroelastic composites for acoustic bandgaps under actuation strains has been carried out (Bortot et al., 2018). All of the above studies have ignored the effects of large deformations by adopting small strain or linearized theories, whereas topology optimization for material design using finite deformation theory is limited to the design of single phase hyperelastic materials for specified Poisson's ratio values (Clausen et al., 2015; Wang et al., 2014).

Motivated by the findings of recent studies (Al-Ketan et al., 2017; Cho et al., 2016; Sabet et al., 2018; Wang et al., 2011), this work is devoted to investigating the use of topology optimization for discovering novel layouts of material phases which enhance the energy dissipation capacity of bi-material polymeric composites. In contrast to previous topology optimization studies for composite design, finite deformation kinematics are adopted to model the experimental behavior reported in Refs. (Al-Ketan et al., 2017; Cho et al., 2016; Sabet et al., 2018; Wang et al., 2011). Different deformation modes are considered and the influence of symmetry, phase volume fraction, and material rate effects on optimized composites is investigated. The paper is organized as follows. In Section 2 the topology optimization framework is detailed, including the multiscale modeling approach used to simulate composite behavior, the material models used to capture the phenomena discussed in Wang et al. (2011), the topology optimization problem formulation, and details needed for sensitivity analysis. In Sections 3 and 4, a number of different optimized composites are obtained and discussed for cases involving different deformation modes, symmetry enforcement, material volume fractions and material rate effects. Section 5 then wraps up with conclusions.

2. Topology optimization framework

To characterize the mechanical behavior of bi-material composites for topology optimization, a computational homogenization approach is utilized. Homogenization is a multiscale method which aims to replace the macroscopic constitutive behavior of a heterogeneous microstructure with that of an effective homogeneous medium. For composites with regular periodic microstructures, heterogeneities can be identified with a representative unit cell (RUC) whose periodic repetition results in a material sample. In this case, the representative unit cell (RUC) provides a microscale domain over which volume averages are taken to obtain the effective homogeneous medium. As this study focuses on the design of such periodic composites, the topology optimization problem will be defined over an RUC domain and periodic repetition of the optimized RUC domain will result in the optimized composite material. The concept of an RUC is illustrated in Fig. 1 where two different microstructures and their corresponding RUCs are shown.

2.1. Multiscale model

To carry out computational homogenization, inhomogeneous distributions of microstructural stress and strain fields within an

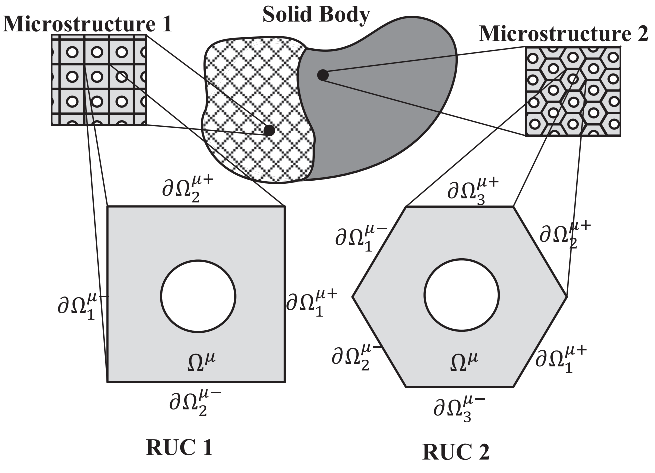

Fig. 1. Solid body with periodic microstructures and corresponding RUCs. Periodic regions of the boundary are shown for each RUC.

RUC are obtained and averaged through the numerical solution of a multiscale model chosen to represent the physical behavior of the material. There are a number of approaches for deriving multiscale models, but the model used for computational homogenization in this study is derived within a recently formulated theoretical framework known as the Method of Multiscale Virtual Power (MMVP). For the sake of brevity details of this derivation will be left out, but the interested reader is directed to Refs. (Alberdi, et al., 2018; Blanco et al., 2016) for specifics.

The multiscale model utilized in this study has kinematics at each scale defined by the displacement field and displacement gradient. Hence, the set of macroscopic kinematical variables is given as $\{\bar{\boldsymbol{u}}, \nabla\bar{\boldsymbol{u}}\}$, where a bar is used to denote macroscopic quantities. Likewise, the set of microscopic kinematical variables is $\{\boldsymbol{u}, \nabla\boldsymbol{u}\} = \{\boldsymbol{u}^H + \tilde{\boldsymbol{u}}, \nabla\boldsymbol{u}^H + \nabla\tilde{\boldsymbol{u}}\}$, with the displacement field at the microscale having been postulated as consisting of a homogeneous part $\boldsymbol{u}^H$ driven by the macroscopic deformation, and a fluctuation part $\tilde{\boldsymbol{u}}$ resulting from microscale heterogeneities. By postulating the homogeneous part $\boldsymbol{u}^H$ as a first order expansion about a macroscopic point $\bar{\boldsymbol{X}}$ located at the RUC centroid, kinematical constraints on the behavior of a periodic microstructure are obtained as

$$\boldsymbol{u}(\boldsymbol{X}) - \boldsymbol{u}(\boldsymbol{X}-\boldsymbol{L}) = \nabla\bar{\boldsymbol{u}}.\boldsymbol{L} \text{ on } \partial\Omega_0^{\mu+} \quad \text{and}$$

$$\bar{\boldsymbol{u}} = \frac{1}{V}\int_{\Omega_0^\mu} \boldsymbol{u}(\boldsymbol{X})dV \tag{1}$$

where V is the total RUC volume. Here, the RUC boundary $\partial\Omega^\mu$ is divided into opposing regions $\partial\Omega^{\mu-}$ and $\partial\Omega^{\mu+}$ such that $\partial\Omega^\mu = \partial\Omega^{\mu+} \cup \partial\Omega^{\mu-}$ and $\partial\Omega^{\mu+} \cap \partial\Omega^{\mu-} = \varnothing$, as shown in Fig. 1, and $\boldsymbol{L} = \boldsymbol{X}^+ - \boldsymbol{X}^-$ for $\boldsymbol{X}^+ \in \partial\Omega^{\mu+}$ and $\boldsymbol{X}^- \in \partial\Omega^{\mu-}$.

The constraints defined in Eq. (1) are then invoked in a variational principle – the Principle of Multiscale Virtual Power (PMVP) – to derive the governing RUC equations and constitutive homogenization relations for volume averaging. The PMVP is a variational extension of the classical Hill-Mandel principle (Hill, 1972; Mandel, 1966) which equates power expenditures at the macro- and microscales. For the model laid out above, this variational statement is

$$\overline{\boldsymbol{P}} : \nabla\delta\bar{\boldsymbol{u}} = \frac{1}{V}\int_{\Omega_0^\mu} \boldsymbol{P} : \nabla\delta\boldsymbol{u}dV \quad \forall\ \delta\boldsymbol{u} \in \mathcal{V}_{kin}, \ \ \nabla\delta\bar{\boldsymbol{u}} \in \mathbb{R}^3 \times \mathbb{R}^3 \tag{2}$$

where $\boldsymbol{P}$ is the first Piola-Kirchhoff stress tensor and $\mathcal{V}_{kin}$ is the space of displacement variations $\delta\boldsymbol{u}$ which satisfy the kinematical constraints in Eq. (1). The variational statement in Eq. (2) can be considered as a stationary principle for some unconstrained functional $\breve{\Pi}$ by employing Lagrange multipliers $(\boldsymbol{\gamma})$ instead of restriction to the constrained space $\mathcal{V}_{kin}$. The stationary conditions for this functional then result in the following multiscale model

Given $\nabla\bar{\boldsymbol{u}}^t$

Find $\boldsymbol{u}(\boldsymbol{X}) = \nabla\bar{\boldsymbol{u}}.\boldsymbol{X} + \tilde{\boldsymbol{u}}(\boldsymbol{X})$ and $\boldsymbol{\gamma}$ such that $\forall\ \delta\boldsymbol{u} \in \boldsymbol{H}^1\left(\Omega_0^\mu\right)$

$$\int_{\Omega_0^\mu} \wp\left(\boldsymbol{F}^t(\boldsymbol{X}, t)\right) : \nabla\delta\boldsymbol{u}dV = -\frac{1}{V}\int_{\partial\Omega_0^{\mu+}} \boldsymbol{\gamma}.(\delta\boldsymbol{u}(\boldsymbol{X}) - \delta\boldsymbol{u}(\boldsymbol{X}-\boldsymbol{L}))dS$$

$$\boldsymbol{u}(\boldsymbol{X}) - \boldsymbol{u}(\boldsymbol{X}-\boldsymbol{L}) - \nabla\bar{\boldsymbol{u}}.\boldsymbol{L} = 0 \text{ on } \partial\Omega_0^{\mu+}$$

$$\frac{1}{V}\int_{\Omega_0^\mu} \boldsymbol{u}(\boldsymbol{X})dV = 0$$

Obtain $\overline{\boldsymbol{P}}\left(\nabla\bar{\boldsymbol{u}}^t\right)$ as

$$\overline{\boldsymbol{P}} = -\frac{1}{V}\int_{\partial\Omega_0^{\mu+}} (\boldsymbol{\gamma} \otimes \boldsymbol{L})dS \tag{3}$$

Here $\nabla\bar{\boldsymbol{u}}^t$ is the history of the macroscale displacement gradient $\nabla\bar{\boldsymbol{u}}$, and the tensor valued functional $\wp$ represents prescribed general microscale constitutive relations, i.e. $\boldsymbol{P}(\boldsymbol{X}, t) = \wp(\boldsymbol{F}^t(\boldsymbol{X},t))$ where $\boldsymbol{F}^t$ denotes the history of the deformation gradient $\boldsymbol{F} = \nabla\boldsymbol{u} + \boldsymbol{I} = \nabla\bar{\boldsymbol{u}} + \nabla\tilde{\boldsymbol{u}} + \boldsymbol{I}$ at each point in the RUC domain. Eq. $(3)_1$ is the weak form of linear momentum balance over the RUC domain in the absence of body forces and Eq. $(3)_3$ precludes rigid body translations of the RUC (see Eq. $(1)_2$). The multiscale model in Eq. (3) defines the constitutive relations $\bar{\boldsymbol{P}}(\nabla\bar{\boldsymbol{u}}^t)$ for an effective homogeneous medium which encapsulates the behavior of the heterogeneous material represented by the RUC.

2.2. Computational homogenization

The multiscale model in Eq. (3) is numerically evaluated using the finite element method, following the framework laid out in (Alberdi, et al., 2018). The resulting set of nonlinear algebraic equations used to approximate RUC equilibrium for a given macroscopic displacement gradient $\nabla\widehat{\bar{\boldsymbol{u}}}$ (here the hat denotes that matrix components are stored in vector form) is thus

$$\boldsymbol{R}(\boldsymbol{u}, \widehat{\boldsymbol{\gamma}}) = \begin{bmatrix} \boldsymbol{R}_1(\boldsymbol{u}, \widehat{\boldsymbol{\gamma}}) \\ \boldsymbol{R}_2(\boldsymbol{u}) \end{bmatrix} = \begin{bmatrix} \boldsymbol{F}_{int}(\boldsymbol{u}) + \boldsymbol{A}^T\widehat{\boldsymbol{\gamma}} \\ \boldsymbol{A}\boldsymbol{u} - \boldsymbol{D}\nabla\widehat{\bar{\boldsymbol{u}}} \end{bmatrix} = \begin{bmatrix} \boldsymbol{0} \\ \boldsymbol{0} \end{bmatrix} \tag{4}$$

where the matrices $\boldsymbol{A}$ and $\boldsymbol{D}$ enforce the two kinematical constraints in Eq. (3) and $\widehat{\boldsymbol{\gamma}}$ is the discrete vector of Lagrange multipliers. In order to account for incompressibility constraints in constitutive behavior, the F-bar finite element formulation is utilized (de Souza Neto, et al., 1996), resulting in the global internal force vector having the following form

$$\begin{aligned} \boldsymbol{F}_{int} &= \mathop{\mathcal{A}}_{e=1}^{n_{ele}} \boldsymbol{F}_{int}^e \\ \boldsymbol{F}_{int}^e &= \int_{\Omega_0^e} r^{a-1}\boldsymbol{B}_e^T\,\tilde{\mathbf{P}}\,dV \end{aligned} \tag{5}$$

Here, $\tilde{\boldsymbol{P}}$ is the first Piola-Kirchhoff stress obtained from evaluating the constitutive relations in terms of the modified deformation gradient $\tilde{\boldsymbol{F}}$. To avoid confusion with macroscopic quantities, a tilde will be used throughout instead of a bar for F-bar quantities. This modified deformation gradient is defined as $\tilde{\boldsymbol{F}} = r^a\boldsymbol{F}$

$$r = \frac{\det\boldsymbol{F}_0}{\det\boldsymbol{F}} \tag{6}$$

where $\boldsymbol{F}_0$ is the deformation gradient evaluated at the element centroid, and the exponent a is 1/2 for two dimensional problems and 1/3 for three dimensional problems.

A displacement control Newton-Raphson algorithm is used to solve the nonlinear system of equations Eq. (4). This requires the Jacobian matrix

$$\mathbf{J} = \begin{bmatrix} \dfrac{\partial\boldsymbol{R}_1}{\partial\boldsymbol{u}} & \dfrac{\partial\boldsymbol{R}_1}{\partial\widehat{\boldsymbol{\gamma}}} \\ \dfrac{\partial\boldsymbol{R}_2}{\partial\boldsymbol{u}} & \dfrac{\partial\boldsymbol{R}_2}{\partial\widehat{\boldsymbol{\gamma}}} \end{bmatrix} = \begin{bmatrix} \boldsymbol{K}_T & \boldsymbol{A}^T \\ \boldsymbol{A} & \boldsymbol{0} \end{bmatrix} \tag{7}$$

where $\boldsymbol{K}_T$ is the global tangent stiffness matrix, defined for the F-bar formulation as

$$\begin{aligned} \boldsymbol{K}_T &= \mathop{\mathcal{A}}_{e=1}^{n_{ele}} \boldsymbol{K}_T^e \\ \boldsymbol{K}_T^e &= \int_{\Omega_0^e} \boldsymbol{B}_e^T\left[\tilde{\mathbb{A}}_T - a\tilde{\mathbb{A}}_T : \left(\tilde{\boldsymbol{F}} \otimes \tilde{\boldsymbol{F}}^{-T}\right) + a\tilde{\boldsymbol{P}} \otimes \tilde{\boldsymbol{F}}^{-T}\right]\boldsymbol{B}_e dV \\ &\quad + \int_{\Omega_0^e} \boldsymbol{B}_e^T\left[ar^{a-1}\tilde{\mathbb{A}}_T : \tilde{\boldsymbol{F}} \otimes \boldsymbol{F}_0^{-T} - ar^{a-1}\tilde{\boldsymbol{P}} \otimes \boldsymbol{F}_0^{-T}\right]\boldsymbol{B}_e^0 dV \end{aligned} \tag{8}$$

with $\tilde{\mathbb{A}}_T$ the algorithmic consistent tangent returned along with the stress $\tilde{\boldsymbol{P}}$ by evaluating the constitutive algorithm in terms of $\tilde{\boldsymbol{F}}$. Following the solution of Eq. (4), the macroscopic stress $\widehat{\bar{\boldsymbol{P}}}$ is obtained in terms of the Lagrange multipliers $\hat{\boldsymbol{\gamma}}$ using the discrete form of Eq. $(3)_4$ as

$$\widehat{\overline{\boldsymbol{P}}} = -\frac{1}{V}\boldsymbol{D}^T\widehat{\boldsymbol{\gamma}} \tag{9}$$

Obtaining the macroscopic stress using Eq. (9) completes the strain-driven computational homogenization procedure wherein the macroscopic displacement gradient $\nabla\bar{\boldsymbol{u}}$ is prescribed and the macroscopic first Piola-Kirchhoff stress is $\bar{\boldsymbol{P}}$ obtained. Additionally, the same discrete system can be used to perform stress-driven computational homogenization (wherein $\bar{\boldsymbol{P}}$ is prescribed and $\nabla\bar{\boldsymbol{u}}$ obtained) and mixed computational homogenization (wherein some components of both $\bar{\boldsymbol{P}}$ and $\nabla\bar{\boldsymbol{u}}$ are prescribed and the remaining components obtained), see (Alberdi, et al., 2018) for details.

Finally, the homogenized tangent moduli tensor $\bar{\mathbb{A}}$ which relates increments of the homogenized first Piola-Kirchhoff stress $\bar{\boldsymbol{P}}$ to increments of the homogenized deformation gradient $\bar{\boldsymbol{F}} = \nabla\bar{\boldsymbol{u}} + \boldsymbol{I}$, i.e. $d\bar{\boldsymbol{P}} = \bar{\mathbb{A}} : d\bar{\boldsymbol{F}}$, can be obtained by linearizing Eq. (9) following the procedure laid out in Alberdi et al. (2018). It is given here as

$$\overline{\mathbb{A}} = -\frac{1}{V}\boldsymbol{Q}^T\boldsymbol{S} \tag{10}$$

where $\boldsymbol{Q} = [\boldsymbol{0} \quad \boldsymbol{D}]^T$ and the matrix $\boldsymbol{S}$ is computed by solving the following system

$$\mathbf{J}\boldsymbol{S} = \boldsymbol{Q} \tag{11}$$

in terms of the Jacobian matrix $\mathbf{J}$ defined in Eq. (7).

2.3. Design parameterization and problem formulation

A density-based parameterization is utilized for topology optimization by assigning each element in the discretized domain a continuous density variable ρ_e $(0 \leq \rho_e \leq 1)$ which is used to represent whether the element contains one material phase $(\rho_e = 0)$ or the other $(\rho_e = 1)$. Because this parameterization allows for the existence of intermediate densities $(0 < \rho_e < 1)$ which do not represent either material phase fully, a material interpolation scheme is needed. In addition to being able to interpolate between different phenomenological models in a consistent way, this scheme should ensure that density values in the final design correspond to distinct material phases. The bi-material interpolation scheme developed in (Alberdi and Khandelwal, 2019) to meet the above criteria is thus adopted in the present study. This interpolation scheme is inspired by classical mixing rules and defines the strain energy ψ within an element as

$$\psi^e = \chi_H(\rho_e)\psi_H + \chi_S(\rho_e)\psi_S \tag{12}$$

where ψ_H and ψ_S are strain energy functions for the harder and softer material phases, respectively. These are scaled by the factors χ_H and χ_S which are functions of the volume fraction of each material phase. In order to ensure that the final topology is free of intermediate density values, penalization in the spirit of the SIMP method (Bendsøe and Sigmund, 1999) is utilized so that the scaling factors χ_H and χ_S contain a penalization parameter p, i.e.

$$\begin{aligned} \chi_H(\rho_e) &= \rho_e^p \\ \chi_S(\rho_e) &= 1 - \rho_e^p \end{aligned} \tag{13}$$

The intent of this study is to design composites which can dissipate the maximum amount of energy through a given volume fraction of hard glassy polymer phase $(\rho_e = 1)$ when the RUC domain is subject to a prescribed macroscopic deformation mode driven by $\nabla\hat{\bar{\boldsymbol{u}}}$. For this purpose, the total plastic work in the RUC domain is utilized as the objective function following the definition in Eq. (19), and a volume fraction constraint is applied to the glassy polymer phase. This results in the following optimization problem

$$\begin{aligned} \min_{\boldsymbol{x}} \quad & f_0(\boldsymbol{x}) = -W^p = -\int_t \int_{\Omega_0^\mu} \dot{w}^{vp} dV dt \\ \text{s.t.} \quad & f_1(\boldsymbol{x}) = \frac{1}{V}\sum_{e=1}^{n_{ele}} \rho_e(\boldsymbol{x}) v_e - V_f \leq 0 \\ & \boldsymbol{R}^k\big(\hat{\boldsymbol{u}}^k, \hat{\boldsymbol{u}}^{k-1}, \boldsymbol{c}^k, \boldsymbol{c}^{k-1}, \boldsymbol{\rho}(\boldsymbol{x})\big) = \boldsymbol{0}, \;\; k = 1, 2, \ldots, n \\ & \boldsymbol{H}^k\big(\hat{\boldsymbol{u}}^k, \hat{\boldsymbol{u}}^{k-1}, \boldsymbol{c}^k, \boldsymbol{c}^{k-1}, \boldsymbol{\rho}(\boldsymbol{x})\big) = \boldsymbol{0}, \;\; k = 1, 2, \ldots, n \\ & \boldsymbol{0} \leq \boldsymbol{x} \leq \boldsymbol{1} \end{aligned} \tag{14}$$

where V is the total volume of the RUC design domain, v_e is the volume of element e and V_f is the prescribed volume fraction of the glassy polymer phase. A density filtering procedure – accounting for the periodicity of the domain – is used to ensure mesh-independency and control the length scale of topological features (Bourdin, 2001; Bruns and Tortorelli, 2001; Li and Khandelwal, 2015). In this case, the design variables $\boldsymbol{x}$ are linearly mapped by the density filtering operator to the vector $\boldsymbol{\rho}$ of density variables, which are obtained as a weighted average of the design variables of neighboring elements.

The system represented in Eq. (14) is a PDE-constrained optimization problem wherein constraint $\boldsymbol{R}^k = \boldsymbol{0}$ represents the global RUC equilibrium equations and $\boldsymbol{H}^k = \boldsymbol{0}$ represents the local integration point constitutive equations. These constraints are enforced implicitly through FEA in a nested approach where the design variables $\boldsymbol{x}$ are updated by the optimizer and then used in FEA. Once FEA has terminated, the objective and constraint functions are evaluated. During FEA, initial value problems describing the evolution of internal variables in path-dependent constitutive models are evaluated by discretizing the deformation history into n time steps. Thus, the implicit constraints $\boldsymbol{R}^k = \boldsymbol{0}$ and $\boldsymbol{H}^k = \boldsymbol{0}$ are enforced at each time step k. At step k, internal variables are updated using previous step and current step information and so the implicit constraints are functionally dependent on this data, represented by a set of global variables $\hat{\boldsymbol{u}}$ and local variables $\boldsymbol{c}$. Furthermore, these constraints are dependent on the density variables $\boldsymbol{\rho}$ through material interpolation (Eq. (12)). Hence, they have the functional form shown in Eq. (14).

2.4. Constitutive modeling

For the bi-material composites investigated in Wang et al. (2011), inclusion of a soft elastomeric phase enhanced energy dissipation in the hard glassy polymer phase by transferring stresses in a way that caused a larger volume of material to experience plastic deformation. This stress transfer mechanism also enhanced the stiffness of the composite compared to a cellular material without the elastomer phase. In order to explore novel bi-material composite designs using topology optimization, the phenomena described above must be captured by the constitutive models utilized within computational homogenization. In Wang et al. (2011), FEA is carried out using an elasto-viscoplastic model for the hard glassy polymer phase and a nearly incompressible hyperelastic model for the soft elastomeric phase. Likewise, in this study the following constitutive models are used.

The elastomer phase is modeled using a nearly incompressible hyperelastic model with strain energy ψ considered to be split into isochoric ψ_{iso} and volumetric ψ_{vol} parts. The isochoric strain energy function is chosen as the regularized Ogden model, defined in terms of the principal stretches $\lambda_a, a = 1, 2, 3$ (i.e. the eigenvalues of the right Cauchy-Green tensor $\boldsymbol{C} = \boldsymbol{F}^T.\boldsymbol{F}$) as

$$\psi_{iso}(\lambda_1,\lambda_2,\lambda_3) = \sum_{p=1}^{N_{mt}} \frac{G_p}{\alpha_p}\left[\overline{\lambda}_1^{\alpha_p} + \overline{\lambda}_2^{\alpha_p} + \overline{\lambda}_3^{\alpha_p} - 3\right]$$
$$\overline{\lambda}_a = J^{-1/3}\lambda_a = \frac{\lambda_a}{(\lambda_1\lambda_2\lambda_3)^{1/3}} = \lambda_a^{\frac{2}{3}}(\lambda_b\lambda_c)^{-\frac{1}{3}} \tag{15}$$

where $J = \det \boldsymbol{F}$ is the volumetric Jacobian, N_{mt} is the number of terms considered in the strain energy function, G_p are constant shear moduli, and α_p are dimensionless constants (Holzapfel, 2000). In Eq. $(15)_2$, $(a,\ b,\ c)$ are cyclic permutations of $(1,\ 2,\ 3)$. For the examples used in this study, only one term is considered in the Ogden strain energy function, i.e. the parameter $N_{mt} = 1$. The shear modulus G_p for this term is set to the shear modulus G and the dimensionless constant $\alpha_p = 2$. This choice of parameters causes the regularized Ogden strain energy function to coincide with the regularized Neo-Hookean strain energy function. The volumetric part of the strain energy is set as $\psi_{vol} = \frac{\kappa}{2}(J-1)^2$, where κ is the bulk modulus.

The glassy polymer phase is modeled using a finite deformation isotropic elasto-viscoplastic model, based on the multiplicative decomposition of the deformation gradient $\boldsymbol{F} = \boldsymbol{F}^e.\boldsymbol{F}^p$, where $\boldsymbol{F}^e$ and $\boldsymbol{F}^p$ are the elastic and plastic parts, respectively, of the total deformation gradient $\boldsymbol{F}$. Following consequences of frame indifference and isotropy, the free energy has the form $\psi(\boldsymbol{b}^e(\boldsymbol{F},\boldsymbol{F}^p),\alpha)$ where $\boldsymbol{b}^e$ is the elastic left Cauchy-Green deformation tensor whose eigenvalues are the elastic principal stretches $\lambda_a^e,\ a = 1, 2, 3$ and α is the accumulated plastic strain. The free energy ψ is further assumed to allow the decomposition $\psi(\boldsymbol{b}^e, \alpha) = \mathcal{W}(\boldsymbol{b}^e) + \mathcal{H}(\alpha)$ into a hyperelastic strain energy function $\mathcal{W} = \mathcal{W}_{iso} + \mathcal{W}_{vol}$ and hardening potential $\mathcal{H}$. Invoking thermodynamic restrictions, the Coleman-Noll procedure (Holzapfel, 2000) then produces the following relation for the Kirchhoff stress tensor $\boldsymbol{\tau}$

$$\boldsymbol{\tau} = 2\frac{\partial\psi}{\partial\boldsymbol{b}^e}.\boldsymbol{b}^e \tag{16}$$

which is related to the first Piola-Kirchhoff stress $\boldsymbol{P}$ as $\boldsymbol{P} = \boldsymbol{\tau}.\boldsymbol{F}^{-T}$. The isochoric and volumetric parts of the strain energy function $\mathcal{W}$ are set to those used for the hyperelastic model defined above, but in terms of the elastic principal stretches $\lambda_a^e,\ a = 1, 2, 3$. A linear isotropic strain hardening model is chosen, so the hardening potential has the quadratic form $\mathcal{H} = \frac{1}{2}K^h\alpha^2$ defined in terms of the hardening coefficient K^h. To complete the constitutive model, flow rules describing the evolution of internal variables are prescribed in an associative manner through the yield function ϕ, chosen here as the von Mises yield function, i.e.

$$\phi = \sqrt{\frac{3}{2}}||\boldsymbol{s}|| - \zeta(\alpha) \tag{17}$$

where $\boldsymbol{s} = \boldsymbol{\tau} - 1/3\mathrm{tr}(\boldsymbol{\tau})\boldsymbol{I}$ is the deviatoric part of the Kirchhoff stress tensor $\boldsymbol{\tau}$ and $\zeta(\alpha) = \sigma_y + \partial\mathcal{H}/\partial\alpha$ is the hardening function. Rate effects are accounted for in a Perzyna-type approach, following the model in (de Souza Neto, et al., 2011; Perić, 1993; Peric and Dettmer, 2003) which defines the following flow rules

$$\boldsymbol{A} \overset{def}{=} \dot{\gamma}\frac{\partial\phi}{\partial\boldsymbol{\tau}} = \dot{\gamma}\sqrt{\frac{3}{2}}\boldsymbol{n}$$
$$\dot{\alpha} = \dot{\gamma}$$
$$\dot{\gamma} = \begin{cases} \dfrac{1}{\mu}\left[\left(\sqrt{\dfrac{3}{2}}\dfrac{||\boldsymbol{s}||}{\zeta}\right)^{\frac{1}{\vartheta}} - 1\right], & \phi \geq 0 \\ 0, & \phi < 0 \end{cases} \tag{18}$$

Here μ is a viscosity parameter (in units of time) and ϑ is a dimensionless rate sensitivity parameter such that the rate-independent von Mises model is recovered from Eq. (18) as $\vartheta \to 0$ or $\mu \to 0$. To characterize the energy dissipated through plastic deformation for this model, the expression for plastic work is obtained as

$$W^p = \int_t\int_{\Omega_0} \dot{w}^{vp}dVdt = \int_t\int_{\Omega_0} \boldsymbol{\tau} : \boldsymbol{A}dVdt \tag{19}$$

where $\dot{w}^{vp}$ is the viscoplastic power density. Numerical implementation of this constitutive model is carried out following the exponential return mapping algorithm discussed in Appendix A. Further details on constitutive modeling for finite deformation elastoplasticity can be found in (Armero, 2017; de Souza Neto, et al., 2011).

Using these constitutive models, an RUC consisting of a hard glassy polymer matrix with circular inclusion of volume fraction $V_f = 0.5$ is analyzed under a uniaxial compression deformation mode. This RUC can be seen as a cross-section of the square cubic (SC) composite design investigated in (Wang et al., 2011), but for the plane strain formulation utilized herein corresponds to an extrusion of the cross-section, i.e. a cylindrical inclusion/void. The material parameters for the elasto-viscoplastic model are set to $E = 3300$, $\nu = 0.33$, $\sigma_y = 105$ and $K^h = 300$. For the hyperelastic model representing the elastomer phase, the shear modulus $G = 3.3$ and bulk modulus $\kappa = 1000$. To simulate a uniaxial compression deformation mode, mixed computational homogenization is carried out using $\nabla\widehat{\bar{\boldsymbol{u}}} = [(\nabla\boldsymbol{u})_{11}\quad 0\quad 0\quad -0.1]$, with $(\nabla\boldsymbol{u})_{11}$ a free component to be found by prescribing $\bar{P}_{11} = 0$. In order to mimic the topology optimization process, a uniform mesh is utilized and elements within the inclusion are considered either to be filled with elastomeric material or empty. Void elements within the empty inclusion are modeled using the strain energy function for the elastomer phase but with the material parameters set to $G = 4.12 \times 10^{-8}$ and $\kappa = 5.48 \times 10^{-8}$.

Fig. 2 reports the total plastic work W^p for both cases and shows the distributions of von Mises stress, accumulated plastic strain α, and plastic work density within the deformed glassy phase. These results reflect the trends reported in Wang et al. (2011), namely that when reinforced with elastomer, stress in the glassy phase is higher and plastic deformation occurs in a greater volume of the glassy phase. Because of this, substantially more energy is dissipated as plastic work, with $W^p = 3.587 \times 10^6$ when reinforced with elastomer as opposed to $W^p = 2.790 \times 10^6$ with void. As these constitutive models are able to capture the phenomena observed in Wang et al. (2011), they are suitable for use in a topology optimization formulation which aims to optimize composites of this type. Unless otherwise noted, the material parameters introduced in this section will be utilized for both material phases in the ensuing optimization examples.

2.5. Initial density distribution

As discussed in (Alberdi and Khandelwal, 2019), a non-uniform distribution of element density values must be used as the initial RUC design in order to have non-uniform sensitivity values. For the examples in this study, the initial density distribution is based on the square cubic (SC) cross-section design analyzed in Section 2.4. That is, the initial distribution consists of a hard elasto-viscoplastic matrix with a circular soft elastomer inclusion. The area of this inclusion is set to satisfy the volume fraction constraint. By relating the area of the circular inclusion to the prescribed volume fraction, results obtained under different volume fraction constraints can be straightforwardly compared. A similar initial density distribution is utilized by Swan and Kosaka (1997), but with the soft phase taken as the matrix and hard phase as the inclusion, so as to represent a fiber reinforced composite.

Elastomer, $W^p = 3.587 \times 10^6$ Void, $W^p = 2.790 \times 10^6$

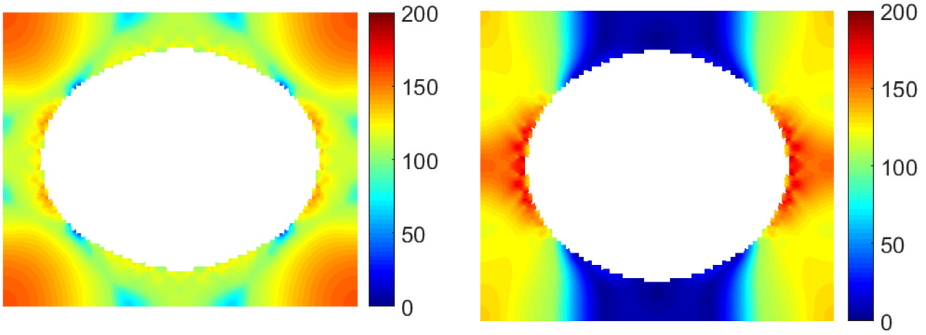

Distribution of von Mises stress in glassy polymer matrix

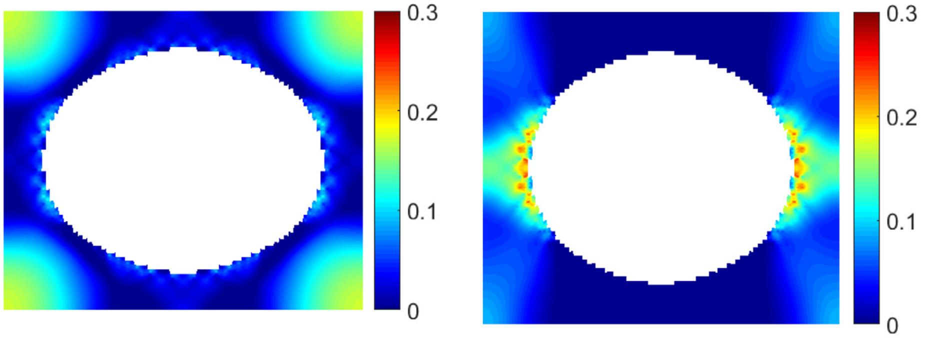

Distribution of accumulated plastic strain (α) in glassy polymer matrix

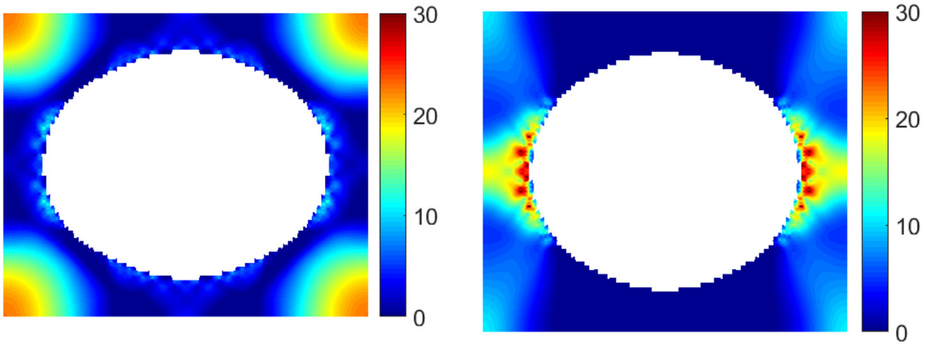

Distribution of plastic work density in glassy polymer matrix

Fig. 2. Result of glassy polymer unit cell subject to uniaxial compression with circular inclusion filled with elastomer and empty.

In order to reduce the bias of the optimizer to the initial density distribution, the density values in the matrix and inclusion are not set to purely elasto-viscoplastic ($\rho_e = 1$) or hyperelastic ($\rho_e = 0$), but intermediate values which approach the values of either material phase. In this case, certain combinations of density values for the matrix and inclusion phases can result in the optimizer converging within a few iterations to a uniform distribution of intermediate density values. Similar undesirable behavior was also observed in Guest and Prevost (2006). To prevent this, the material interpolation scheme should be defined in such a way that a uniform distribution of intermediate density values is less optimal than any given topology. In order to ensure that the plastic work in elements with intermediate density values is appropriately penalized, the tensor $\boldsymbol{A}$ (Eq. $(18)_1$) in the viscoplastic power density $\dot{w}^{vp}$ used to evaluate the total plastic work W^p in the objective function is scaled by a factor χ_A, i.e.

$$\dot{w}^{vp} = \boldsymbol{\tau}^{VP} : (\chi_A \boldsymbol{A}) = \chi_A \dot{\gamma} \sqrt{\frac{3}{2}} \boldsymbol{\tau}^{VP} : \boldsymbol{n} \tag{20}$$

where use is made of Eq. $(18)_1$ and $\boldsymbol{\tau}^{VP}$ and $\boldsymbol{n}$ are the Kirchhoff stress and flow vector from the elasto-viscoplastic model. Note that the Kirchhoff stress tensor in this expression remains interpolated through the element strain energy function in Eq. (12). The scaling factor is set to $\chi_A = \rho_e^{p_A}$ with p_A being an extra penalization parameter. With the appropriate choice of p_A, a uniform distribution of intermediate density values will be penalized such that optimizer will be able to determine discrete topologies.

2.6. Sensitivity analysis

In order to exploit the use of gradient-based nonlinear programming algorithms to solve the topology optimization problem in Eq. (14), accurate sensitivity information is needed, which can only be obtained by accounting for the implicit constraints $\boldsymbol{R}^k = \boldsymbol{0}$ and $\boldsymbol{H}^k = \boldsymbol{0}$ at each time step k. The general adjoint sensitivity analysis framework formulated in Alberdi et al. (2018) for such path-dependent PDE constrained optimization problems is thus utilized herein. Given a response function f with the general functional form $f(\boldsymbol{x}) = F(\widehat{\boldsymbol{u}}^1, \dots, \widehat{\boldsymbol{u}}^n, \boldsymbol{c}^1, \dots, \boldsymbol{c}^n, \boldsymbol{x})$, the sensitivity $df/d\boldsymbol{x}$ is obtained by first solving the following system of equations for the adjoint variables $\boldsymbol{\lambda}^k$ and $\boldsymbol{\mu}^k$

$$
n^{th}\ step: \begin{cases} \dfrac{\partial F}{\partial \widehat{\boldsymbol{u}}^n} + \boldsymbol{\lambda}^{n^T} \dfrac{\partial \boldsymbol{R}^n}{\partial \widehat{\boldsymbol{u}}^n} + \boldsymbol{\mu}^{n^T} \dfrac{\partial \boldsymbol{H}^n}{\partial \widehat{\boldsymbol{u}}^n} = \boldsymbol{0} \\ \dfrac{\partial F}{\partial \boldsymbol{c}^n} + \boldsymbol{\lambda}^{n^T} \dfrac{\partial \boldsymbol{R}^n}{\partial \boldsymbol{c}^n} + \boldsymbol{\mu}^{n^T} \dfrac{\partial \boldsymbol{H}^n}{\partial \boldsymbol{c}^n} = \boldsymbol{0} \end{cases}
$$

$$
k^{th}\ step: \begin{cases} \dfrac{\partial F}{\partial \widehat{\boldsymbol{u}}^k} + \boldsymbol{\lambda}^{k+1^T} \dfrac{\partial \boldsymbol{R}^{k+1}}{\partial \widehat{\boldsymbol{u}}^k} + \boldsymbol{\mu}^{k+1^T} \dfrac{\partial \boldsymbol{H}^{k+1}}{\partial \widehat{\boldsymbol{u}}^k} \\ \quad + \boldsymbol{\lambda}^{k^T} \dfrac{\partial \boldsymbol{R}^k}{\partial \widehat{\boldsymbol{u}}^k} + \boldsymbol{\mu}^{k^T} \dfrac{\partial \boldsymbol{H}^k}{\partial \widehat{\boldsymbol{u}}^k} = \boldsymbol{0} \\ \dfrac{\partial F}{\partial \boldsymbol{c}^k} + \boldsymbol{\lambda}^{k+1^T} \dfrac{\partial \boldsymbol{R}^{k+1}}{\partial \boldsymbol{c}^k} \\ \quad + \boldsymbol{\mu}^{k+1^T} \dfrac{\partial \boldsymbol{H}^{k+1}}{\partial \boldsymbol{c}^k} + \boldsymbol{\lambda}^{k^T} \dfrac{\partial \boldsymbol{R}^k}{\partial \boldsymbol{c}^k} + \boldsymbol{\mu}^{k^T} \dfrac{\partial \boldsymbol{H}^k}{\partial \boldsymbol{c}^k} = \boldsymbol{0} \end{cases}
$$

$$
k = n-1, \dots, 2, 1 \tag{21}
$$

As application of the density filter mapping design variables $\boldsymbol{x}$ to density variables $\boldsymbol{\rho}$ is straightforwardly accounted for by applying the chain rule, the derivative $df/d\boldsymbol{\rho}$ is sought. After solving Eq. (21) by starting at step n and ending at step 1, the sensitivity $df/d\boldsymbol{\rho}$ is evaluated as

$$
\frac{df}{d\boldsymbol{\rho}} = \frac{\partial F}{\partial \boldsymbol{\rho}} + \sum_{k=1}^{n} \left(\boldsymbol{\lambda}^{k^T} \frac{\partial \boldsymbol{R}^k}{\partial \boldsymbol{\rho}} + \boldsymbol{\mu}^{k^T} \frac{\partial \boldsymbol{H}^k}{\partial \boldsymbol{\rho}} \right) \tag{22}
$$

The following derivatives are thus needed for Eqs. (21) and (22):

$$
For\ \boldsymbol{R}^k: \begin{cases} \dfrac{\partial \boldsymbol{R}^k}{\partial \boldsymbol{\rho}} \\ \dfrac{\partial \boldsymbol{R}^k}{\partial \widehat{\boldsymbol{u}}^k} \\ \dfrac{\partial \boldsymbol{R}^k}{\partial \widehat{\boldsymbol{u}}^{k-1}} \\ \dfrac{\partial \boldsymbol{R}^k}{\partial \boldsymbol{c}^k} \\ \dfrac{\partial \boldsymbol{R}^k}{\partial \boldsymbol{c}^{k-1}} \end{cases}, \quad For\ \boldsymbol{H}^k: \begin{cases} \dfrac{\partial \boldsymbol{H}^k}{\partial \boldsymbol{\rho}} \\ \dfrac{\partial \boldsymbol{H}^k}{\partial \widehat{u}^k} \\ \dfrac{\partial \boldsymbol{H}^k}{\partial \widehat{\boldsymbol{u}}^{k-1}} \\ \dfrac{\partial \boldsymbol{H}^k}{\partial \boldsymbol{c}^k} \\ \dfrac{\partial \boldsymbol{H}^k}{\partial \boldsymbol{c}^{k-1}} \end{cases}, \quad For\ F: \begin{cases} \dfrac{\partial \boldsymbol{F}}{\partial \boldsymbol{\rho}} \\ \dfrac{\partial \boldsymbol{F}}{\partial \widehat{u}^k} \\ \dfrac{\partial \boldsymbol{F}}{\partial \boldsymbol{c}^k} \end{cases} \tag{23}
$$

These are obtained by specifying the set of global $\widehat{\boldsymbol{u}}$ and local $\boldsymbol{c}$ state variables and their corresponding constraint equations. For the problems considered in this study, the global state variables and constraints are based on the discrete governing RUC equations Eq. (4), i.e.

$$
\widehat{\boldsymbol{u}}^k = \begin{bmatrix} \boldsymbol{u}^k \\ \widehat{\boldsymbol{\gamma}}^k \end{bmatrix}; \quad \boldsymbol{R}^k = \begin{bmatrix} \boldsymbol{R}_1^k \\ \boldsymbol{R}_2^k \end{bmatrix} = \begin{bmatrix} \mathop{\mathcal{A}}\limits_{e=1}^{n_{ele}} \boldsymbol{F}_{int}^{e^k} + \boldsymbol{A}^T \widehat{\boldsymbol{\gamma}}^k \\ \boldsymbol{A}\boldsymbol{u}^k - \boldsymbol{D}\nabla\widehat{\widehat{\boldsymbol{u}}} \end{bmatrix} \tag{24}
$$

For the F-bar elements used to discretize the RUC domain in this study, the element internal force vector is $\boldsymbol{F}_{int}^{e^k} = \sum_{r=1}^{n_{ipt}} w_r r_{e_r}^{k^{a-1}} \boldsymbol{B}_{e_r}^T \tilde{\boldsymbol{P}}_{e_r}^k$. Here $r_{e_r}^k$ is the deformation gradient ratio defined in Eq. (6) for integration point r, $a = 1/2$ for the plane strain case and w_r is the weight of the r^{th} integration point. Considering four node plane strain F-bar elements with $n_{ipt} = 4$ integration points, the chosen local variables $\boldsymbol{c}^k$ are represented in vector form as

$$
\boldsymbol{c}^k = \begin{bmatrix} \boldsymbol{c}_1^k \\ \vdots \\ \boldsymbol{c}_{n_{ele}}^k \end{bmatrix} \quad \text{with} \quad \boldsymbol{c}_e^k = \begin{bmatrix} \boldsymbol{c}_{e_1}^k \\ \boldsymbol{c}_{e_2}^k \\ \boldsymbol{c}_{e_3}^k \\ \boldsymbol{c}_{e_4}^k \end{bmatrix} \quad \text{and} \quad \boldsymbol{c}_{e_r}^k = \begin{bmatrix} \boldsymbol{b}_{e_r}^{e^k} \\ \alpha_{e_r}^k \\ \Delta\gamma_{e_r}^k \end{bmatrix} \tag{25}
$$

The local constraint equations corresponding to these variables thus have the form

$$
\boldsymbol{H}^k = \begin{bmatrix} \boldsymbol{H}_1^k \\ \vdots \\ \boldsymbol{H}_{n_{ele}}^k \end{bmatrix} = \boldsymbol{0} \quad \text{with} \quad \boldsymbol{H}_e^k = \begin{bmatrix} \boldsymbol{H}_{e_1}^k \\ \boldsymbol{H}_{e_2}^k \\ \boldsymbol{H}_{e_3}^k \\ \boldsymbol{H}_{e_4}^k \end{bmatrix} \quad \text{and} \quad \boldsymbol{H}_{e_r}^k = \begin{bmatrix} \boldsymbol{h}_{e_{r1}}^k \\ h_{e_{r2}}^k \\ h_{e_{r3}}^k \end{bmatrix} \tag{26}
$$

and the residual equations $\boldsymbol{H}_{e_r}^k$ at each integration point r follow from the constitutive algorithm discussed in Appendix A. For a given integration point at the elastic step, these equations are

$$
\boldsymbol{H}_{e_r}^k = \begin{cases} \boldsymbol{h}_{e_{r1}}^k = \boldsymbol{b}_{e_r}^{e^k} - \boldsymbol{b}_{e_r}^{e,tr} = \boldsymbol{0} \\ h_{e_{r2}}^k = \alpha_{e_r}^k - \alpha_{e_r}^{k-1} = 0 \\ h_{e_{r3}}^k = \Delta\gamma_{e_r}^k = 0 \end{cases} \tag{27}
$$

and for a given integration point at the viscoplastic step, they are

$$
\boldsymbol{H}_{e_r}^k = \begin{cases} \boldsymbol{h}_{e_{r1}}^k = \boldsymbol{b}_{e_r}^{e^k} - \boldsymbol{b}_{e_r}^{e,tr}.\exp\left[-2\Delta t \boldsymbol{A}_{e_r}^k\right] = \boldsymbol{0} \\ h_{e_{r2}}^k = \alpha_{e_r}^k - \alpha_{e_r}^{k-1} - \Delta\gamma_{e_r}^k = 0 \\ h_{e_{r3}}^k = \sqrt{\dfrac{3}{2}} s_{e_r}^{VP^k} \left(\dfrac{\Delta t}{\mu \Delta\gamma_{e_r}^k + \Delta t} \right)^{\vartheta} - \zeta\left(\alpha_{e_r}^k\right) = 0 \end{cases} \tag{28}
$$

where $\Delta t = t_k - t_{k-1}$. The derivatives in Eq. (23) needed to complete the sensitivity analysis based on these definitions are given in Appendix B, and an example verifying correct implementation of this sensitivity analysis is presented in Appendix C.

3. Optimized composite designs

In this section, the topology optimization framework laid out in Section 2 is applied to explore performance-optimized material layouts which exploit the stress transfer mechanisms discussed in Wang et al. (2011) and illustrated in Section 2.4 to enhance the energy dissipation capacity of composites. For all of the optimization problems carried out in this section, a displacement control scheme is utilized with an adaptive step-size Newton-Raphson strategy (Crisfield, 1991) to solve the strain-driven microscale system in Eq. (4), with convergence criterion based on the global energy residual, $\text{abs}(\boldsymbol{R}^T \boldsymbol{\Delta}\widehat{\boldsymbol{u}}) \le 10^{-12}$. Optimization is carried out using the Method of Moving Asymptotes (MMA) (Svanberg, 1987) with default algorithmic parameters and terminated after 300 total iterations. The penalization parameters p and p_A are both set to 3 and the filter radius utilized is $r_{min} = 3 \times ms$ where ms is the size of each element in the uniform mesh. In all of the figures showing optimized composite topologies, the elasto-viscoplastic phase is shown in red while the hyperelastic phase is shown in blue. The in-house Matlab based finite element solver CPSSL-FEA developed at the University of Notre Dame is used to perform both the optimization and FEA.

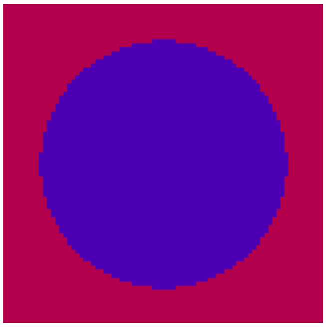

Fig. 3. Initial density distribution for topology optimization when inclusion has a volume fraction $V_f = 0.5$.

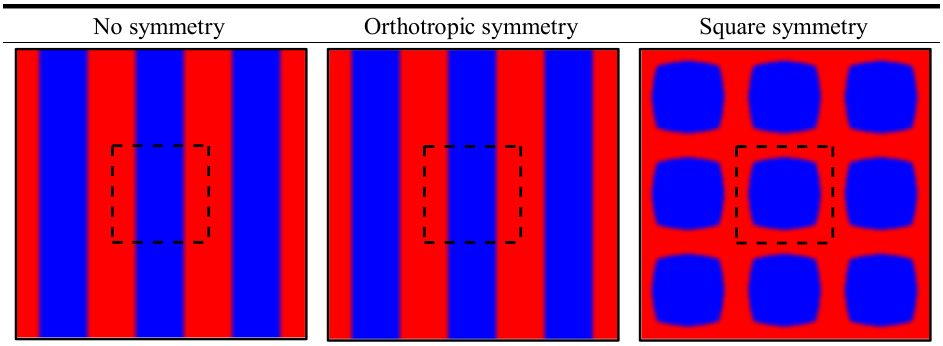

$W^p = 9.106 \times 10^6$ $W^p = 9.106 \times 10^6$ $W^p = 5.516 \times 10^6$

(i) Uniaxial compression

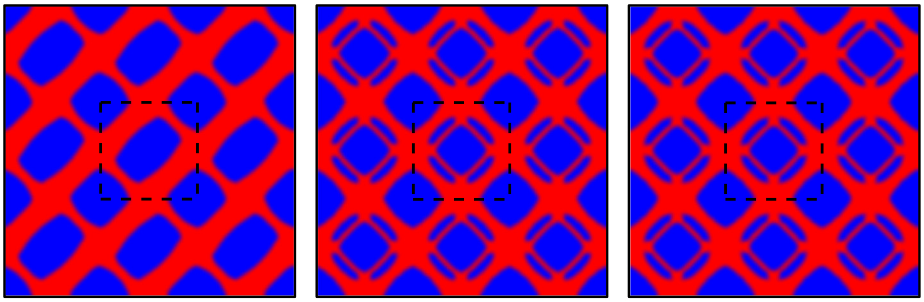

$W^p = 1.400 \times 10^7$ $W^p = 1.392 \times 10^7$ $W^p = 1.383 \times 10^7$

(ii) Simple shear

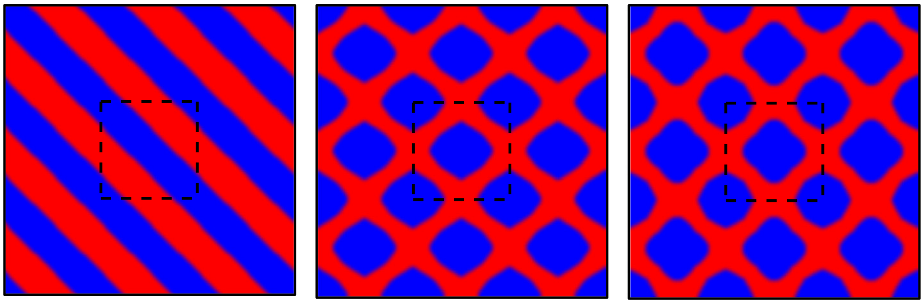

$W^p = 6.144 \times 10^6$ $W^p = 4.196 \times 10^6$ $W^p = 3.926 \times 10^6$

(iii) Combined shear and compression – case 1

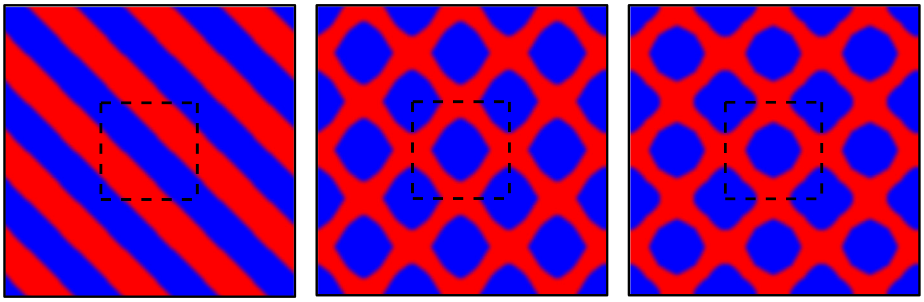

$W^p = 6.144 \times 10^6$ $W^p = 4.196 \times 10^6$ $W^p = 3.926 \times 10^6$

(iv) Combined shear and compression – case 2

Fig. 4. Optimized composites obtained under different deformation modes and symmetry cases using $V_f = 0.5$.

3.1. Deformation modes and symmetry

In this section, a square RUC domain of dimensions 1000 by 1000 is discretized into an 80 × 80 mesh of plane strain F-bar elements and optimized under a number of different macroscopic deformation modes. The deformation modes considered include: (i) uniaxial compression under 20% strain ($\nabla\widehat{\boldsymbol{u}} = [0 \quad 0 \quad 0 \quad -0.2]$); (ii) simple shear under 25% strain ($\nabla\widehat{\boldsymbol{u}} = [0 \quad 0.25 \quad 0.25 \quad 0]$); and two cases of combined shear and compression, (iii) ($\nabla\widehat{\boldsymbol{u}} = [-0.1 \quad 0.2 \quad 0 \quad 0]$), and (iv) ($\nabla\widehat{\boldsymbol{u}} = [0 \quad 0 \quad 0.2 \quad -0.1]$). Geometric symmetry lines which correspond to macroscale elastic orthotropy and square symmetry in the linear elastic regime are prescribed (see discussion in (Neves et al., 2000)), and optimization for each deformation mode is carried out using these two symmetry cases in addition to the case where no symmetry is enforced. The prescribed volume fraction of the hard glassy polymer phase is set

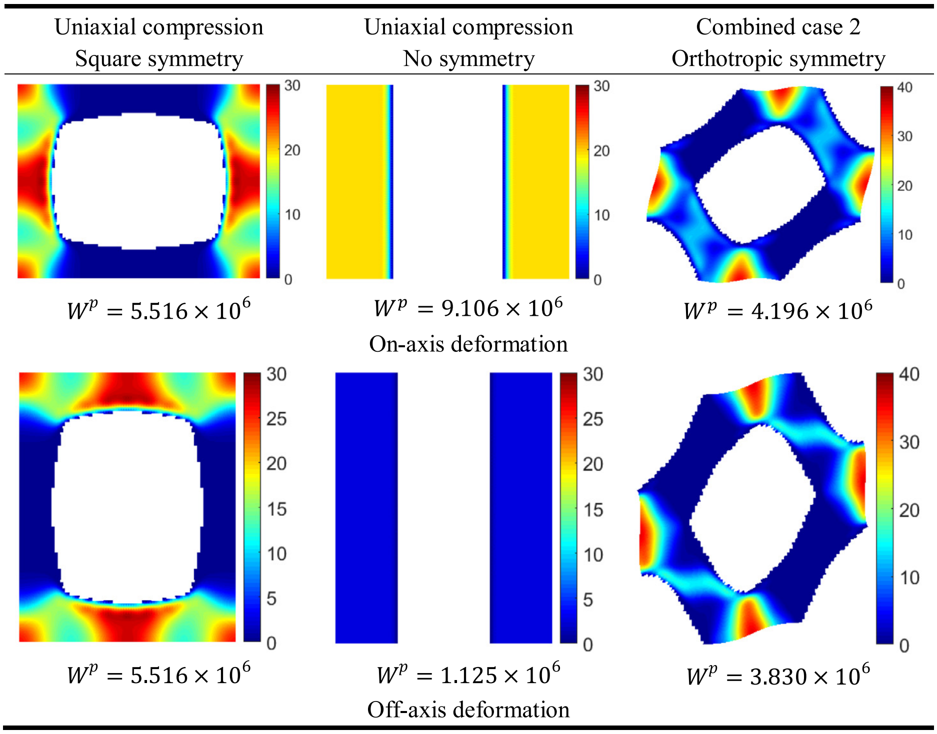

Fig. 5. Plastic work density distributions in glassy phase of deformed optimized RUC under uniaxial compression and combined shear and compression (case 2) for different symmetry cases subject to on-axis and off-axis deformation.

to $V_f = 0.5$ and Fig. 3 gives the initial density distribution. In this distribution, density values for the hard glassy polymer matrix are $\rho_H = 0.7$ while density values for the soft elastomer inclusion are $\rho_S = 0.3$.

The optimized composites obtained under each deformation mode and symmetry case are shown in Fig. 4 with the RUC outlined in black dashed lines. The total plastic work in the RUC domain (W^p) is also reported in this figure. It can be seen that when no symmetry is enforced the optimized composites for all but the simple shear deformation mode resemble lamellar composites. Through the investigations carried out on bi-material polymeric composites in Cho et al. (2016) and Sabet et al. (2018) it was concluded that the stiffness is enhanced in composites with a connected hard phase rather than a disperse lamellar structure. However, these results suggest that for certain deformation modes the use of lamellar composites leads to improved energy dissipation capacity. This trend is similar to the results reported in Andreasen et al. (2014) for the design of viscoelastic composites. A downside of this type of composite topology is that the high degree of anisotropy means being subject to an off-axis deformation mode can result in drastically decreased performance. Indeed, in Wang et al. (2011) it is mentioned that composite designs with a lower degree of anisotropy can provide an advantage in terms of performance under arbitrary deformation modes.

The anisotropy of composites can of course be reduced by increasing the degree of geometric symmetry and this is borne out in the optimized composites shown in Fig. 4 under different symmetry cases. Here it can be seen that enforcing symmetry results in optimized composites with a well-connected glassy phase, more closely resembling those in Wang et al. (2011). While increasing the degree of symmetry reduces optimality in terms of total plastic work values under the prescribed deformation mode, it offers an improvement in performance under deformation modes aligned along other axes. This is illustrated in Fig. 5, where the distribution of plastic work density within the glassy phase of the deformed optimized RUCs obtained under uniaxial compression and combined shear and compression (case 2) with different symmetries is shown for both on-axis and off-axis deformation. The total plastic work in the RUC domain (W^p) is also provided. Here, on-axis refers to the deformation modes prescribed during optimization (i.e. $\nabla\widehat{\boldsymbol{u}} = [0 \quad 0 \quad 0 \quad -0.2]$ and $\nabla\widehat{\boldsymbol{u}} = [0 \quad 0 \quad 0.2 \quad -0.1]$, respectively) and off-axis to the same deformation modes but with the axes of application flipped (i.e. $\nabla\widehat{\boldsymbol{u}} = [-0.2 \quad 0 \quad 0 \quad 0]$ and $\nabla\widehat{\boldsymbol{u}} = [-0.1 \quad 0.2 \quad 0 \quad 0]$, respectively). For the case of uniaxial compression, plastic work density distributions are shown for the cases of no symmetry and square symmetry. For the case of combined shear and compression, plastic work density distributions are only provided for the case of orthotropic symmetry since this deformation mode is the same as that used for case 1 of combined shear and compression and the optimized composites obtained under the other symmetry cases match.

When the degree of symmetry is reduced, the plastic work values under off-axis deformation decrease due to the glassy polymer phase being utilized in an inefficient manner. This inefficient usage is especially clear for uniaxial compression, as the reduction in plastic work is 87.6%. However, when square symmetry is enforced the plastic work values match under on-axis and off-axis deformation. This can be seen in Fig. 4 for the combined shear and compression deformation mode by comparing the two cases. Thus, the tradeoff in terms of optimal design performance under a given deformation mode and more robust performance under general deformations can be controlled by enforcing different degrees of geometric symmetry.

Finally, to demonstrate the advantages of using topology optimization to design composites of this type, Fig. 6a shows the convergence curve for the shear deformation mode with square symmetry enforced. Keeping in mind that the initial density distribution used is a cross-section of an SC topology (albeit under plane strain conditions), this convergence shows the level of improvement that can be achieved by optimizing the RUC topology. Furthermore, Fig. 6b compares the evolution of macroscopic von Mises stress for this optimized RUC to that of the SC RUC with discrete

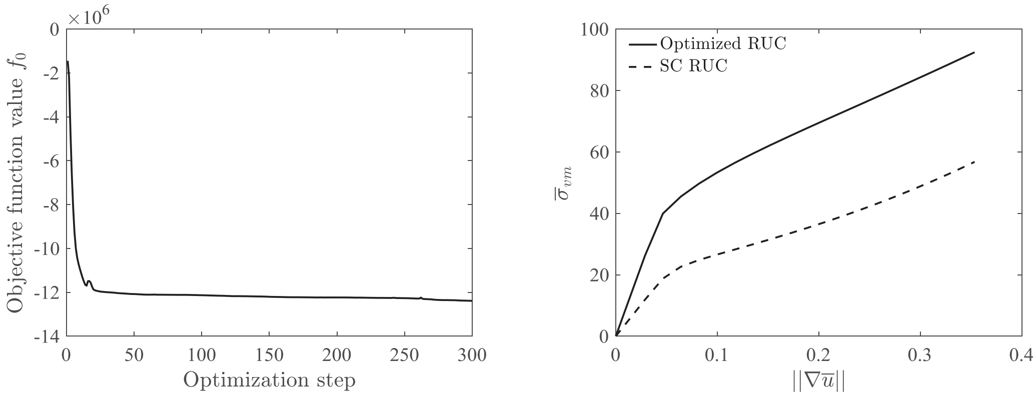

(a) Convergence (b) Macroscopic stress strain behavior

Fig. 6. Convergence curve and comparison of macroscopic stress-strain behavior of optimized composite RUC obtained under simple shear with square symmetry.

glassy polymer and soft elastomer phases (i.e. $\rho_H = 1$ and $\rho_S = 0$) under the same shear deformation mode. These results show that a topology optimization-based approach for designing bi-material composites can lead to significant improvement in design performance.

3.2. Volume fraction

Next, the influence of phase volume fraction on optimized composite designs is investigated by considering case (iv) from Section 3.1, i.e. the combined shear and compression deformation mode ($\nabla\hat{\bar{\boldsymbol{u}}} = [0 \quad 0 \quad 0.2 \quad -0.1]$). Two new volume fractions are considered for the hard glassy polymer phase, i.e. $V_f = 0.35$ and $V_f = 0.65$. The initial density distribution again has the density values for the hard glassy polymer matrix set to $\rho_H = 0.7$ and density values for the elastomer inclusion set to $\rho_S = 0.3$ but the area of the inclusion differs based on the prescribed volume fraction. Fig. 7 shows the optimized composites obtained when enforcing square symmetry for these two volume fractions as well as that obtained in Section 3.1 using $V_f = 0.5$. It can be seen that the optimized composites are the same topologically, but the thickness of the glassy polymer members varies with volume fraction. Accordingly, as the volume fraction of the glassy phase is increased, the energy dissipation capacity of the composite (i.e. the plastic work) increases. Also shown in Fig. 7 is the distribution of plastic work density within the glassy phase of the deformed optimized RUCs for each volume fraction. It can be seen that for the different volume fractions, the composites make use of the same deformation mechanisms to maximize the plastic work, resulting in very similar distributions. Hence, the topology of material phases appears to have a greater influence on energy dissipation capacity than does volume fraction.

The volume fraction of constituent phases influences not only the energy dissipation capacity of the composite but also the degree of anisotropy. In Cho et al. (2016) the influence of volume fraction of the hard phase on the degree of anisotropy in connected and disperse composite topologies was investigated. It was found that in composites with a connected hard phase the

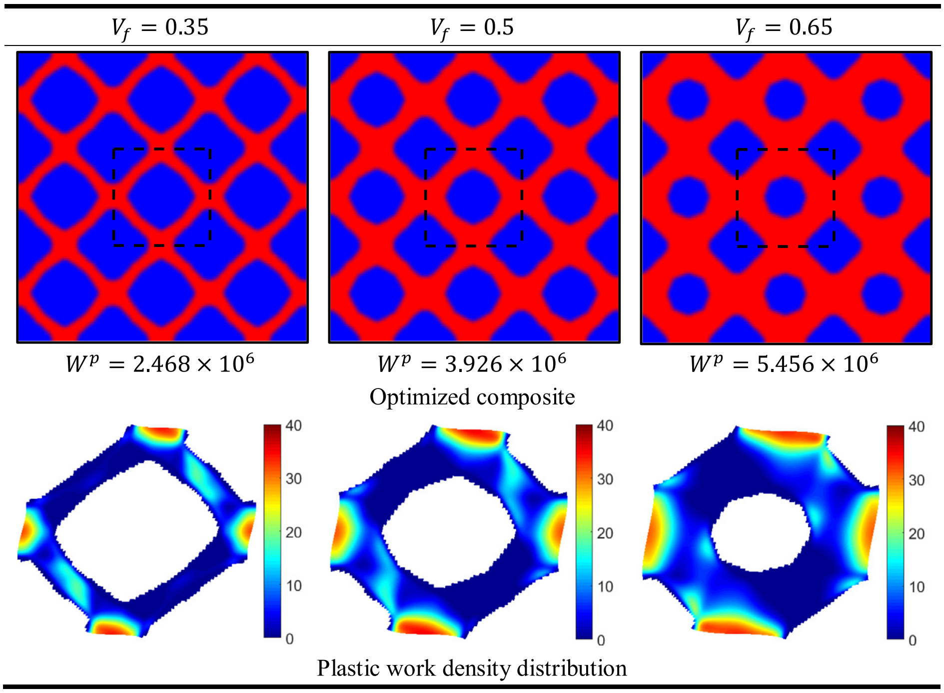

Fig. 7. Optimized composites and plastic work density distributions in glassy phase of deformed optimized RUC under combined shear and compression and square symmetry using different volume fractions of glassy phase.

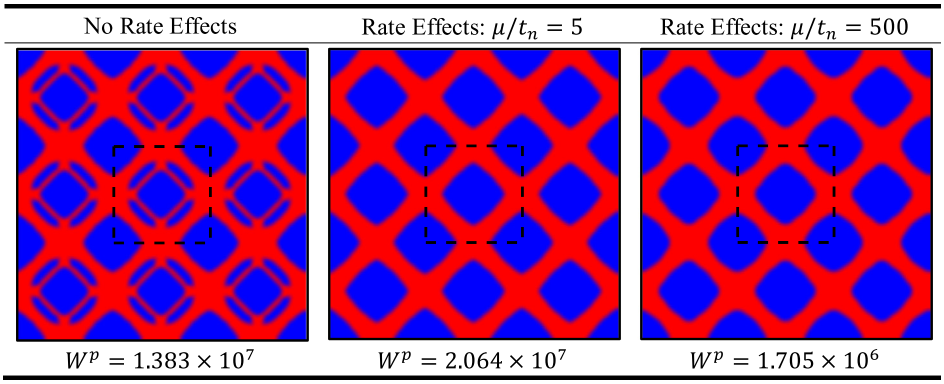
No Rate Effects | Rate Effects: $\mu/t_n = 5$ | Rate Effects: $\mu/t_n = 500$

$W^p = 1.383 \times 10^7$ | $W^p = 2.064 \times 10^7$ | $W^p = 1.705 \times 10^6$

Fig. 8. Optimized composites under simple shear and orthotropic symmetry with different viscoplastic rate effects in glassy phase.

degree of anisotropy decreases as the volume fraction is increased, while in composites with a disperse hard phase the anisotropy increases with increasing volume fraction. In composites with cubic symmetry (square symmetry for the plane strain case), there are three independent elastic constants and the degree of anisotropy can be determined in terms of these constants as

$$a = \frac{2C_{44}}{C_{11} - C_{12}} \tag{29}$$

where the constant C_{11} is a measure of the stiffness under longitudinal compression, C_{12} is a measure of the stiffness under transverse expansion and C_{44} is a measure of the stiffness under shearing. The anisotropy ratio a thus contains information on how the composite stiffness changes with orientation of the RUC, and $a = 1$ corresponds to isotropic behavior. This ratio can be calculated for optimized composites in terms of the components of the homogenized tangent moduli in Eq. (10), but calculated for the initial linear elastic response (see discussion on calculation of initial tangent moduli in (Alberdi and Khandelwal, 2019)) when square symmetry is enforced. The anisotropy ratios for the optimized composites shown in Fig. 7 are $a = 9.717$ when $V_f = 0.35$, $a = 4.061$ when $V_f = 0.5$ and $a = 2.032$ when $V_f = 0.65$. Hence, the anisotropy decreases with increasing volume fraction, mirroring the trends observed in (Cho et al., 2016) for composites with a connected hard phase.

3.3. Rate effects

In the previous optimization examples, the elasto-viscoplastic model parameters are set so that the behavior is rate-independent (i.e. the rate sensitivity parameter $\vartheta = 0$). This mimics the type of loading considered in Wang et al. (2011) where the deformation is applied slowly so that rate effects are negligible. As glassy polymer materials show rate-dependent plastic behavior, however, the influence of this behavior on the optimized composite topologies is now investigated. Note that elastomeric materials may have non-negligible rate dependent viscoelastic behavior at high rates, but this behavior is not captured in the hyperelastic model used for this phase. The simple shear deformation mode from Section 3.1 (i.e. $\nabla\hat{\boldsymbol{u}} = [0 \quad 0.25 \quad 0.25 \quad 0]$) is considered with orthotropic symmetry enforced and optimization is carried out for two different cases considering rate effects with a volume fraction constraint $V_f = 0.5$ on the glassy phase. The rate effects for these two cases are enabled by setting $\vartheta = 1$ and controlled by setting the ratio between the viscosity parameter and total time of deformation (μ/t_n) to 5 and 500, which correspond low-to-moderate and high rates of deformation, respectively. Fig. 8 compares the optimized composites obtained for these two cases to that from Section 3.1 where no rate effects are considered. It can be seen that the consideration of rate effects results in different compos-

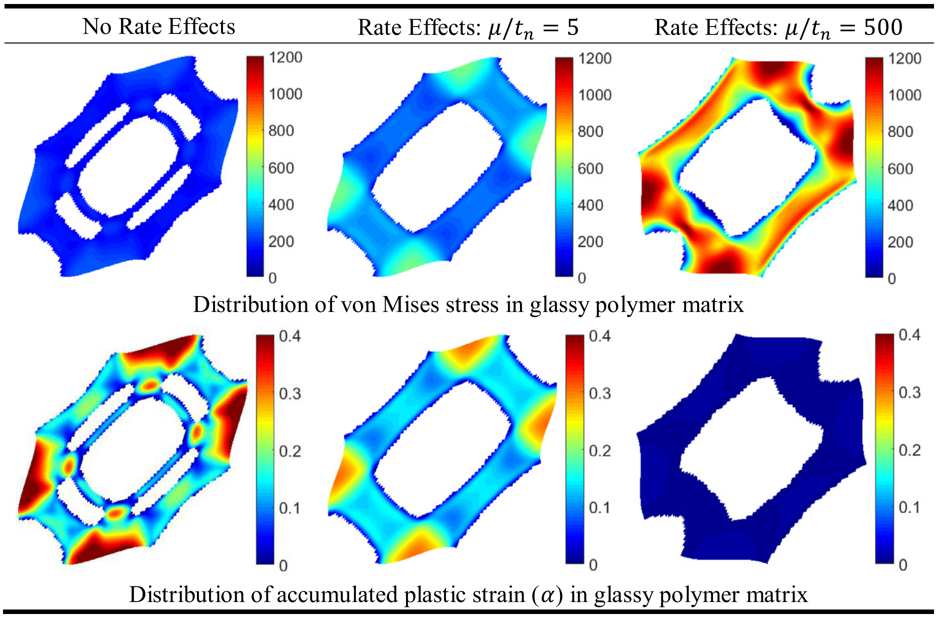
No Rate Effects | Rate Effects: $\mu/t_n = 5$ | Rate Effects: $\mu/t_n = 500$

Distribution of von Mises stress in glassy polymer matrix

Distribution of accumulated plastic strain (α) in glassy polymer matrix

Fig. 9. Distributions of von Mises stress and accumulated plastic strain in glassy phase of deformed optimized RUC obtained with different viscoplastic rate effects.

ite topologies. The optimized composites obtained under the two different rate cases are the same topologically, but have slight differences in their shapes.

Of note is that the total plastic work in the optimized composite obtained using $\mu/t_n = 5$ is the highest of the three cases, while that in the optimized composite obtained using $\mu/t_n = 500$ is the lowest. This can be explained by looking at the distributions of von Mises stress and accumulated plastic strain in the glassy polymer phase of the deformed topologies, as shown in Fig. 9. Here it can be seen that increasing the rate of deformation results in higher stress values, but lowers the amount of plastic flow. At the low-to-moderate rate captured by $\mu/t_n = 5$, the stress is much higher compared to the rate-independent case while significant plastic flow still occurs. As the plastic work depends on both the stress level and the amount of plastic flow, this case results in the highest amount of plastic work. At the high rate captured by $\mu/t_n = 500$ the stress is much higher than in the other two cases, but the total plastic work is much reduced due to the negligible plastic flow. As such rate effects influence how the material phases should be arranged to increase energy dissipation capacity, they must be considered for design scenarios where composites are subject to rapid loading times.

4. Soft energy dissipating phase

For the glassy polymer and elastomer materials investigated in Wang et al. (2011) and modeled in the previous sections, the hard material phase provides both the stiffness and energy dissipation capacity. The role of the soft phase is thus to provide the stress transfer mechanisms which allow a greater volume of the hard phase to be exploited to enhance these properties. This phenomenon is reflected in optimized composite topologies where the glassy polymer phase forms a connected frame which is reinforced by the elastomer phase. As nonlinear problems are highly dependent on material parameters, it is worth investigating how changing these parameters can affect the response and optimization of bi-material composites. Specifically, an alternative way to combine hard and soft phases in a composite is to have the hard phase provide stiffness while the soft phase provides energy dissipation capacity. This approach is now investigated by using the hyperelastic model as the hard phase and the elasto-viscoplastic model as the soft phase. The parameters of the hyperelastic phase are set to $G = 1241$ and $\kappa = 3235$ while the parameters of the elasto-viscoplastic phase are set to $E = 2500$, $\nu = 0.38$, $f_y = 20$ and $K^h = 125$. The scaling factors χ_H and χ_S remain defined as in Eq. (13), but will be swapped for this case in the sensitivity derivative expressions presented in Appendix B. Hence $\rho_e = 1$ corresponds to the hyperelastic hard phase while $\rho_e = 0$ corresponds to the elasto-viscoplastic soft phase. To carry out topology optimization with these materials, the scaling factor χ_A in Eq. (20) is set to 1 – as the optimizer can find discrete topologies without extra penalization – and the penalization parameter is kept as $p = 3$. Analysis and optimization are carried out as discussed at the beginning of Section 3.

4.1. Square RUC domain

The square RUC domain utilized in Section 3 is again considered. The initial density distribution is set to the SC cross-section with inclusion scaled by the prescribed volume fraction, but the matrix material is now initialized as the hard hyperelastic phase while the inclusion is initialized as the soft elasto-viscoplastic phase. Initial density values for the hard and soft phases are set to $\rho_H = 0.9$ and $\rho_S = 0.1$, respectively, and the volume fraction constraint on the soft energy dissipating elasto-viscoplastic phase uses $V_f = 0.5$. Again, a filter radius of $r_{min} = 3 \times ms$ is utilized. In the optimized composites shown below the colors remain set so that red represents the elasto-viscoplastic (soft) phase while blue represents the hyperelastic (hard) phase.

The optimized composites and distributions of plastic work density within each deformed optimized RUC are shown in Fig. 10 for three different deformation modes: uniaxial compres-

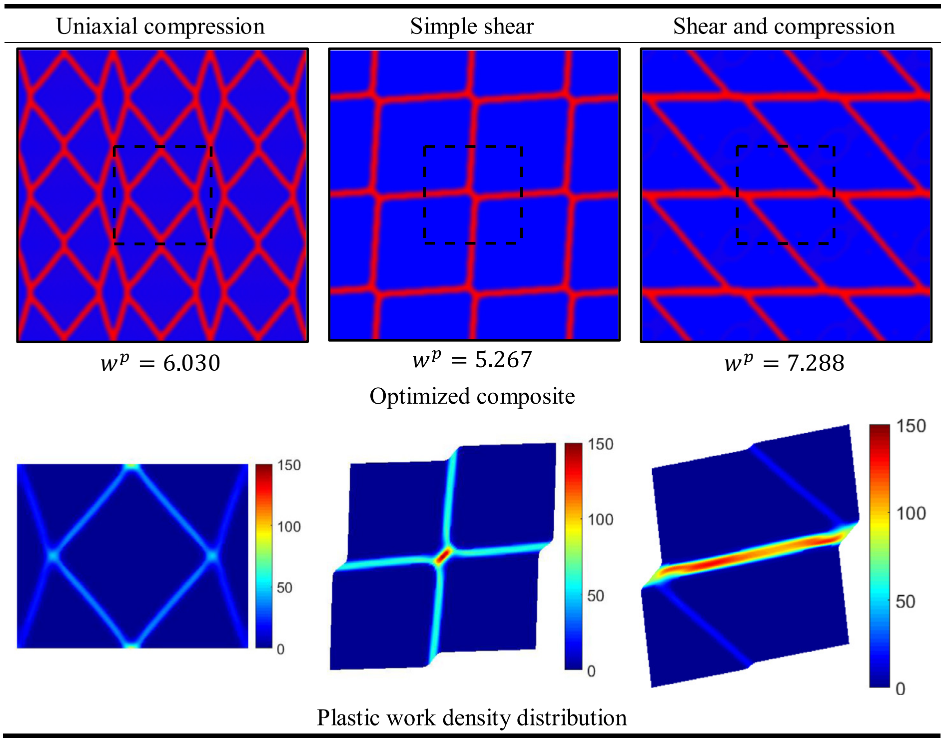

Fig. 10. Optimized composites and plastic work density distributions in deformed configuration of optimized square RUC under different deformation modes with hard hyperelastic phase and soft elasto-viscoplastic phase.

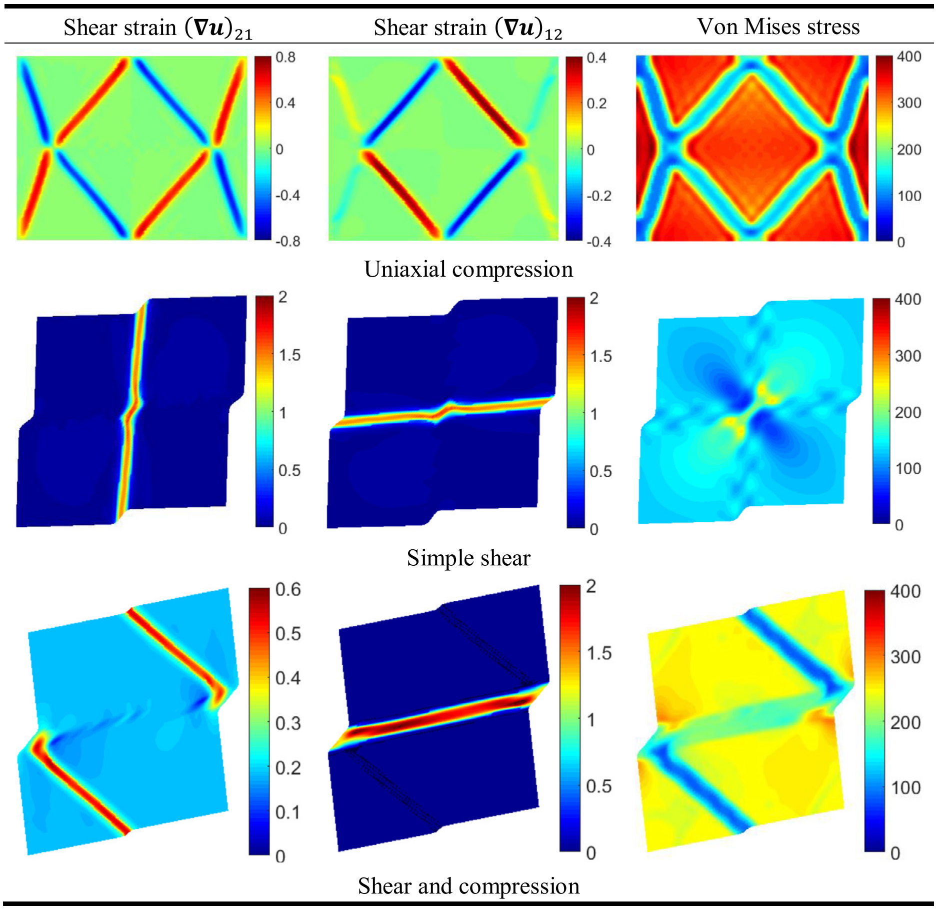

Fig. 11. Distributions of shear strain components and von Mises stress in deformed configuration of optimized square RUC under different deformation modes with hard hyperelastic phase and soft elasto-viscoplastic phase.

sion under 20% strain ($\nabla\hat{\boldsymbol{u}} = [0 \quad 0 \quad 0 \quad -0.2]$), simple shear under 10% strain ($\nabla\hat{\boldsymbol{u}} = [0 \quad 0.1 \quad 0.1 \quad 0]$), and combined shear and compression ($\nabla\hat{\boldsymbol{u}} = [-0.1 \quad 0.2 \quad 0 \quad 0]$). Also shown is the plastic work capacity w^p, i.e. the plastic work W^p divided by the RUC volume V. For all three deformation modes, the optimized composites consist of hard phase inclusions within a matrix of the soft phase. Hence, these optimized composites are disperse, having an unconnected hard phase which is in stark contrast to the well-connected optimized composites obtained previously. In fact, for this combination of hard and soft phases the volume fraction constraint on the soft energy dissipating phase is not even active. The percentage of soft phase utilized is 30.0% for the uniaxial compression case, 12.7% for the simple shear case and 15.7% for the combined shear and compression case. This suggests that using a smaller percentage of the soft energy dissipating phase results in superior energy dissipation capacity than if a greater volume of this phase was utilized.

Looking at the distributions of plastic work density in the optimized composites (Fig. 10), it can be seen that a large amount of energy dissipation occurs throughout the entire soft phase. In fact, this arrangement of material phases appears to have been determined so as to purposefully induce localized strain concentrations wherein a large amount of energy can be dissipated. This is carried out by allowing the hard inclusions to deform relative to each other such that shear strains are localized within the thin layers of the soft phase, leading to high shear stress values and resulting plastic work. For example, Fig. 11 shows the distribution of the shear components of the microscale displacement gradient $\nabla \boldsymbol{u}(\boldsymbol{X})$ throughout the RUC, and it can be clearly seen that shear strains are localized in the soft phase. Also shown in Fig. 11 is the distribution of the von Mises stress throughout the RUC, where the higher stress values in the hard inclusions indicate that this phase is providing stiffness to the composite. This localization of strains leading to high energy dissipation thus explains why utilizing a lower volume of soft phase is considered more optimal. Designs of this type mimic natural materials which exploit similar phenomena in their arrangement of material phases (Barthelat, 2015). Hence, radically different phenomena are exploited to optimize composites when the hard phase provides stiffness and the soft phase energy dissipation capacity than when the hard phase provides both.

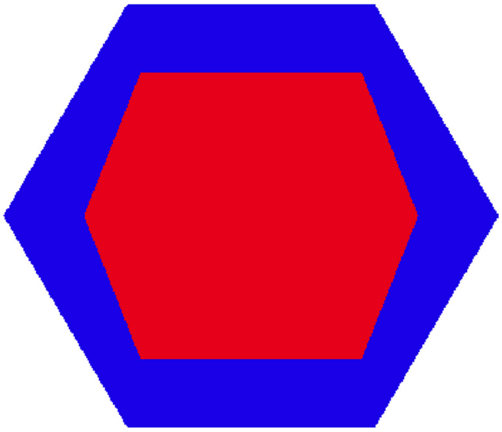

Fig. 12. Initial density distribution for hexagonal RUC domain when inclusion has a volume fraction $V_f = 0.5$.

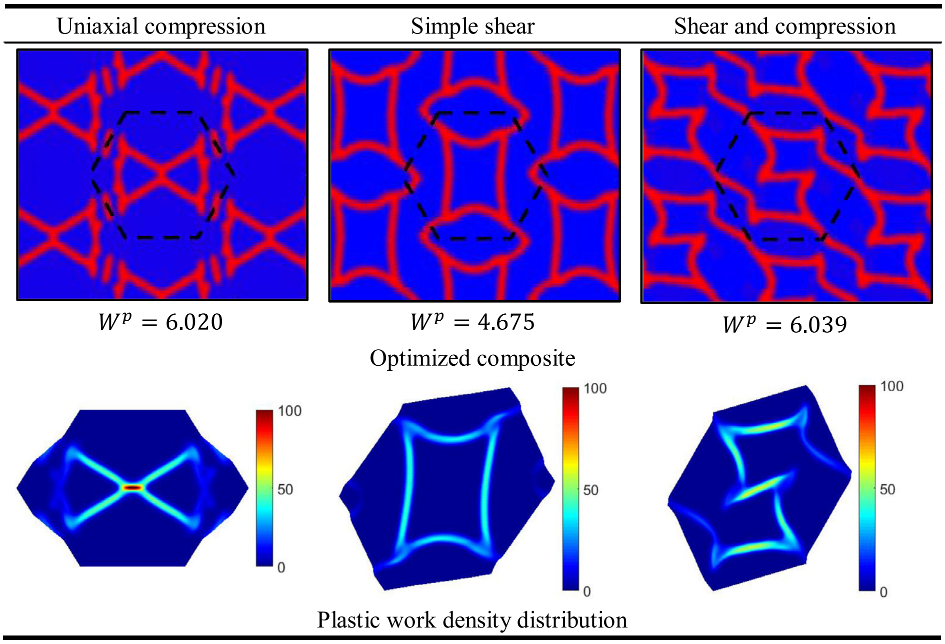

Fig. 13. Optimized composites and plastic work density distributions in deformed configuration of optimized hexagonal RUC under different deformation modes with hard hyperelastic phase and soft elasto-viscoplastic phase.

4.2. Hexagonal RUC domain

Next, the same material phases and deformation modes are considered, but using a hexagonal RUC domain (RUC 2 in Fig. 1) instead of a square RUC domain. Each side of this domain has a dimension of 1000 and 6400 non-uniform plane strain F-bar elements are used for discretization. The filter radius used for topology optimization with this domain is set to 80 and the initial density distribution is shown in Fig. 12, where the hexagonal inclusion of elasto-viscoplastic phase is sized so as to meet the prescribed volume fraction $V_f = 0.5$. Initial density values for the hard and soft phases are again set to $\rho_H = 0.9$ and $\rho_S = 0.1$, respectively.

Optimized topologies obtained under each of the three deformation modes from Section 4.1 are shown in Fig. 13 along with the plastic work density distributions within the deformed RUC configurations and the plastic work capacity w^p. It can be seen that distinct topologies are obtained as compared to those with the square RUC in Fig. 10, despite the same deformation modes and similar initial density distributions. This is due to the fact that the hexagonal RUC represents a different type of periodicity and causes the RUC to deform in a different manner (as shown in the deformed RUC domain in Fig. 13). However, the optimized topologies follow the same trends as when the square RUC is utilized, i.e. the soft energy dissipating elasto-viscoplastic phase is arranged so as to induce areas of highly localized plastic work. Again, in these examples the volume fraction constraint is not active as using a small amount of the elasto-viscoplastic phase results in greater energy dissipation capacity.

5. Conclusions

A topology optimization framework for the purpose of discovering novel performance-optimized designs of bi-material composites with enhanced energy dissipation is explored in this study. This work is motivated by the numerical and experimental studies in Refs. (Al-Ketan et al., 2017; Cho et al., 2016; Sabet et al., 2018; Wang et al., 2011) which combine a hard glassy polymer phase with a soft elastomer phase to enhance the stiffness, toughness and energy dissipation capacity of composites. The topology optimization examples investigated herein show the ability of the framework to exploit the physical phenomena reported in Wang et al. (2011) to improve energy dissipation capacity. Using an initial topology corresponding to an extruded cross-section of the square cubic composite investigated in Wang et al. (2011), significant improvements in energy dissipation capacity are obtained under different prescribed deformation modes. These results suggest that a topology optimization-based approach for designing bi-material composites can lead to significantly improved designs.

A key takeaway concerns the tradeoff between the use of highly specialized anisotropic composite topologies and more robust topologies with a lower degree of anisotropy. The former result in very high energy dissipation capacity for a specific deformation mode while the latter can perform more optimally under general deformations. Enforcing geometric symmetry leads to composites with a lower degree of anisotropy and a well-connected hard glassy polymer phase, and the dependence of the anisotropy on the volume fraction of this hard phase is illustrated. Additionally, varying the volume fractions assigned to different material phases during optimization illustrates the outsized role that the topological arrangement of these phases plays in increasing energy dissipation capacity as compared to phase volume fraction. The effects of material rate dependence on optimized composite behavior are also shown. These effects follow similar trends as those observed in the design of multi-material structures with material rate effects (Alberdi and Khandelwal, 2019). The design of composites with a soft phase providing energy dissipation capacity and hard phase providing stiffness is also carried out. Optimized designs highlight how vastly different phenomena are exploited to dissipate energy in optimized composites of this type. Namely, the hard hyperelastic phase is arranged in a disperse manner so as to induce localized strain concentrations in the soft elasto-viscoplastic phase.

There are numerous ways that the work presented herein can be extended. First, elasto-viscoplastic models which consider damage accumulation can be incorporated into the optimization framework in an approach similar to Li et al. (2018). This is especially relevant for problems considering a soft elasto-viscoplastic phase, as the optimized topologies obtained in Section 4 exploit highly localized plastic work which can lead to damage accumulation and eventual material failure. Second, as composite strength is often dictated by interface properties, homogenization and optimization techniques which take the material interface into account should be considered, see for example, the works (Firooz and Javili, 2019; Saeb et al., 2019; Saeb et al., 2019). The authors are currently pursuing these avenues.

Declaration of Competing Interest

The authors declare that they have no known competing financial interests or personal relationships that could have appeared to influence the work reported in this paper.

CRediT authorship contribution statement

Ryan Alberdi: Investigation, Software, Visualization, Validation, Formal analysis, Data curation, Writing - original draft. **Kapil Khandelwal:** Conceptualization, Methodology, Software, Supervision, Project administration, Writing - review & editing.

Acknowledgements

The presented work is supported in part by the US National Science Foundation through grant CMMI-1762277. Any opinions, findings, conclusions, and recommendations expressed in this paper are those of the authors and do not necessarily reflect the views of the sponsors.

Supplementary materials

Supplementary material associated with this article can be found, in the online version, at doi:10.1016/j.ijsolstr.2020.02.006.

Appendix A. Exponential return mapping algorithm

This appendix presents the exponential return mapping algorithm used to numerically implement the elasto-viscoplastic material model discussed in Section 2.3. For time step $m+1$ at integration point r of element e, given information includes the current and previous step deformation (characterized by $\tilde{\boldsymbol{F}}_{e_r}^{m+1}$ and $\tilde{\boldsymbol{F}}_{e_r}^{m}$) and the previous step internal variables ($\mathcal{J}_{e_r}^{m} = \{\boldsymbol{b}_{e_r}^{e^m}, \alpha_{e_r}^{m}\}$). The purpose of the constitutive algorithm is to calculate the current step stress $\tilde{\boldsymbol{P}}_{e_r}^{m+1}$, internal variables $\mathcal{J}_{e_r}^{m+1}$ and the consistent tangent modulus $\tilde{\mathbb{A}}_T$ needed to evaluate the tangent matrix in Eq. (8). The exponential return mapping algorithm detailed in this appendix is presented with the superscript removed from variables at the current time step $m+1$ and no reference made to element or integration point number. Likewise, the bar is removed from any of the F-bar quantities so that the algorithm is presented independently from the type of element used.

Making use of the relations for the plastic distortion-rate tensor $\boldsymbol{L}^p = \dot{\boldsymbol{F}}^p.\boldsymbol{F}^{p-1} = \boldsymbol{F}^{e-1}.\boldsymbol{l}^p.\boldsymbol{F}^e$ and the polar decomposition $\boldsymbol{F}^e = \boldsymbol{V}^e.\boldsymbol{R}^e$, the rate equation for the plastic part of the deformation gradient $\boldsymbol{F}^p$ can be written as

$$\dot{\mathbf{F}}^{p} = \boldsymbol{R}^{e^T}.\boldsymbol{A}.\boldsymbol{R}^e.\boldsymbol{F}^p \tag{A.1}$$

This rate equation is numerically approximated using the exponential mapping integrator, giving

$$\boldsymbol{F}^p = \exp\left[\Delta t \boldsymbol{R}^{e^T}.\boldsymbol{A}.\boldsymbol{R}^e\right].\boldsymbol{F}_n^p = \boldsymbol{R}^{e^T}.\exp\left[\Delta t \boldsymbol{A}\right].\boldsymbol{R}^e.\boldsymbol{F}_n^p \tag{A.2}$$

The exponential map integrator is used as it preserves the incompressibility of plastic flow, i.e. it ensures that $\det \boldsymbol{F}^p = 1$. Using Eq. (A.2) along with the definitions $\boldsymbol{F}^e = \boldsymbol{F}.\boldsymbol{F}^{p-1}$ and $\boldsymbol{b}^e = \boldsymbol{V}^{e2}$ results in the following discrete flow rule for $\boldsymbol{b}^e$

$$\boldsymbol{b}^e = \exp\left[-2\Delta t \boldsymbol{A}\right].\boldsymbol{F}.\boldsymbol{F}_n^{-1}.\boldsymbol{b}_n^e.\boldsymbol{F}_n^{-T}.\boldsymbol{F}^T = \boldsymbol{b}^{e,tr}.\exp\left[-2\Delta t \boldsymbol{A}\right] \tag{A.3}$$

where the trial elastic left Cauchy-Green deformation tensor is defined as $\boldsymbol{b}^{e,tr} = \Delta\boldsymbol{F}.\boldsymbol{b}_n^e.\Delta\boldsymbol{F}^T$ with $\Delta\boldsymbol{F} = \boldsymbol{F}.\boldsymbol{F}_n^{-1}$ and can be seen to depend on the given previous step information $\boldsymbol{b}_n^e$ and $\boldsymbol{F}_n$ and current step information $\boldsymbol{F}$. The discrete flow rule Eq. (A.3) can be greatly simplified by considering its evaluation in the space spanned by the elastic left principal directions $\boldsymbol{l}_a^e, a = 1, 2, 3$. In this space,

$$\begin{aligned} \boldsymbol{b}^e &= \sum_a^3 \lambda_a^{e^2} \boldsymbol{l}_a^e \otimes \boldsymbol{l}_a^e \\ \boldsymbol{b}^{e,tr} &= \sum_a^3 \lambda_a^{e,tr^2} \boldsymbol{l}_a^{e,tr} \otimes \boldsymbol{l}_a^{e,tr} \end{aligned} \tag{A.4}$$

Given the coaxiality between $\boldsymbol{b}^e$ and $\boldsymbol{\tau}$ resulting from the assumption of isotropy, together with the coaxiality between $\boldsymbol{b}^e$ and $\boldsymbol{A}$ resulting from the assumption of associativity, the principal directions $\boldsymbol{l}_a^e$ coincide with $\boldsymbol{l}_a^{e,tr}$. Thus, in principal space, Eq. (A.3) is

$$\lambda_a^{e^2} = \exp\left[-2\Delta\gamma\sqrt{\frac{3}{2}}n_a\right]\lambda_a^{e,tr^2}, \quad a = 1, 2, 3 \tag{A.5}$$

where n_a are the principal components of the flow vector $\boldsymbol{n}$. Taking the natural logarithm of this expression results finally in the discrete flow rule for the logarithmic elastic principal stretches $\varepsilon_a^e = \ln\lambda_a^e$, i.e.

$$\varepsilon_a^e = \varepsilon_a^{e,tr} - \Delta\gamma\sqrt{\frac{3}{2}}n_a, \quad a = 1, 2, 3 \tag{A.6}$$

which can be seen to coincide with the discrete flow rule for the elastic strains in the small strain case (de Souza Neto et al., 2011).

Complementing the discrete flow rule in Eq. (A.6) with the discrete flow rule for the accumulated plastic strain α obtained by utilizing a backward Euler integration thus provides the necessary equations for carrying out the return mapping algorithm. The first step of this algorithm is the elastic trial step which is performed as follows

$$\text{Given}: \quad \boldsymbol{F}, \ \boldsymbol{b}^{e,tr} = \boldsymbol{F}.\boldsymbol{F}_n^{-1}.\boldsymbol{b}_n^e.\boldsymbol{F}_n^{-T}.\boldsymbol{F}^T, \ \alpha^{tr} = \alpha_m$$

Evaluate τ_a^{tr} using the trial elastic principal stretch values $\lambda_a^{e,tr}$ in Eq. (15). Compute

$$\begin{aligned} \boldsymbol{s}^{tr} &= \mathbb{P}_{dev}^{s}\boldsymbol{\tau}^{tr} \\ \mathrm{q}^{tr} &= K^h\alpha^{tr} \\ \phi^{tr}\left(\boldsymbol{\tau}^{tr}, q^{tr}\right) &= \sqrt{\frac{3}{2}}\|\boldsymbol{s}^{tr}\| - \left(\sigma_y + q^{tr}\right) \end{aligned} \tag{A.7}$$

with $\boldsymbol{\tau}^{tr} = [\tau_1^{tr} \quad \tau_2^{tr} \quad \tau_3^{tr}]^T$, $\boldsymbol{s}^{tr} = [s_1^{tr} \quad s_2^{tr} \quad s_3^{tr}]^T$, and $\|\boldsymbol{s}^{tr}\| = \sqrt{s_1^{tr2} + s_2^{tr2} + s_3^{tr2}}$. The matrix $\mathbb{P}_{dev}^{s} = \boldsymbol{I} - \mathbf{1}/3$ where $\mathbf{1}$ is a matrix whose entries are all 1.

If $\phi^{tr} \leq 0$ then the current step is an elastic step and the following elastic updates are made

$$\begin{aligned} \boldsymbol{b}^e &= \boldsymbol{b}^{etr}, \ \alpha = \alpha^{tr}, \ \boldsymbol{\tau} = \boldsymbol{\tau}^{tr} \\ \mathbb{A}_T &= \mathbb{A} \end{aligned} \tag{A.8}$$

where $\mathbb{A}$ is the matrix form of the tangent moduli tensor $\mathbb{A} = \partial^2\psi/\partial\boldsymbol{F}\partial\boldsymbol{F}$ for the strain energy function defined in Eq. (15).

Else, if $\phi^{tr} > 0$ then plastic flow is occurring in this step and the algorithm proceeds to Step 2, the viscoplastic return mapping step. In this step, the initial value problem defined by the flow rules given in Eq. (18) must be evaluated numerically. Making use of Eq. (A.6), the discrete update equations for the time step $\Delta t = t - t_m$ are

$$\begin{aligned} \varepsilon_a^e &= \varepsilon_a^{e,tr} - \Delta\gamma\sqrt{\frac{3}{2}}n_a, \;\; a = 1,2,3 \\ \alpha &= \alpha_m + \Delta\gamma \\ \Delta\gamma &= \frac{1}{\mu}\left[\left(\sqrt{\frac{3}{2}}\frac{\|\boldsymbol{s}\|}{\zeta}\right)^{\frac{1}{\vartheta}} - 1\right]\Delta t \\ n_a &\overset{def}{=} \frac{s_a}{\|\boldsymbol{s}\|} \end{aligned} \tag{A.9}$$

Combining Eqs. $(A.9)_2$ and $(A.9)_3$ thus results in the nonlinear algebraic system

$$\boldsymbol{R} = \begin{bmatrix} \boldsymbol{R}_1 \\ R_2 \end{bmatrix} = \begin{bmatrix} \boldsymbol{\varepsilon}^e - \boldsymbol{\varepsilon}^{etr} + \Delta\gamma\sqrt{\frac{3}{2}}\boldsymbol{n} \\ \Delta\gamma - \frac{\Delta t}{\mu}\left[\left(\sqrt{\frac{3}{2}}\frac{\|\boldsymbol{s}\|}{\zeta(\Delta\gamma)}\right)^{\frac{1}{\epsilon}} - 1\right] \end{bmatrix} = \begin{bmatrix} \boldsymbol{0} \\ 0 \end{bmatrix} \tag{A.10}$$

which is solved for the unknowns $\boldsymbol{X} = [\boldsymbol{\varepsilon}^e \quad \Delta\gamma]^T$ using the Newton-Raphson method with tangent matrix

$$\frac{d\boldsymbol{R}}{d\boldsymbol{X}} = \begin{bmatrix} \boldsymbol{I} + \frac{\Delta\gamma}{\|\boldsymbol{s}\|}\sqrt{\frac{3}{2}}\left(\mathbb{P}^s_{dev} - \boldsymbol{n}\otimes\boldsymbol{n}\right)\boldsymbol{B} & \sqrt{\frac{3}{2}}\boldsymbol{n} \\ \left(\frac{\Delta t}{\mu\Delta\gamma + \Delta t}\right)^{\vartheta}\sqrt{\frac{3}{2}}\boldsymbol{n}^T\boldsymbol{B} & -\left(\sqrt{\frac{3}{2}}\left(\frac{\Delta t}{\mu\Delta\gamma + \Delta t}\right)^{\vartheta}\frac{\vartheta\mu\|\boldsymbol{s}\|}{\mu\Delta\gamma + \Delta t} + K^h\right) \end{bmatrix} \tag{A.11}$$

Here, $\boldsymbol{B}$ is a matrix containing the terms $\partial\tau_a/\partial\varepsilon_b^e, \; a, b = 1, 2, 3$. The converged values of ε_a^e are used to obtain the elastic principal stretches λ_a^e and by extension $\boldsymbol{b}^e$. The converged values τ_a are used to obtain $\boldsymbol{\tau}$ and the first Piola-Kirchhoff stress tensor is calculated as $\boldsymbol{P} = \boldsymbol{\tau}.\boldsymbol{F}^{-T}$. The algorithmic consistent tangent modulus $\mathbb{A}_T$ can then be calculated in component form as

$$\mathbb{A}_{ijkl} = J\mathfrak{a}_{ipkr}F_{jp}^{-1}F_{lr}^{-1} \tag{A.12}$$

where the spatial moduli tensor a is given as

$$J\mathfrak{a} = \frac{\partial\boldsymbol{\tau}}{\partial\boldsymbol{b}^{e,tr}} : \left(\boldsymbol{I}\boxtimes\boldsymbol{b}^{e,tr^T} + \boldsymbol{b}^{e,tr}\boxdot\boldsymbol{I}\right) - \boldsymbol{\tau}\boxdot\boldsymbol{I} \tag{A.13}$$

and the products $\boxtimes$ and $\boxdot$ between two second order tensors are defined as $(\boldsymbol{A}\boxtimes\boldsymbol{B})_{ijkl} = A_{ik}B_{jl}$ and $(\boldsymbol{A}\boxdot\boldsymbol{B})_{ijkl} = A_{il}B_{jk}$. The term $\partial\boldsymbol{\tau}/\partial\boldsymbol{b}^{e,tr}$ is computed in principal space using data from the constitutive Newton-Raphson routine as

$$\left[\frac{\partial\tau_a}{\partial b_b^{e,tr}}\right]_{a,b=1,2,3} = \boldsymbol{B}\boldsymbol{D}_{11}$$

with

$$\begin{bmatrix} \mathrm{d}\mathbf{R} \\ \mathrm{d}\mathbf{X} \end{bmatrix}^{-1} = \begin{bmatrix} \boldsymbol{D}_{11} & \boldsymbol{D}_{12} \\ \boldsymbol{D}_{21} & \boldsymbol{D}_{22} \end{bmatrix} \tag{A.14}$$

and then brought to physical space for use in Eq. (A.13). This completes the exponential return mapping algorithm.

Appendix B. Derivatives for sensitivity analysis

Based on the definition of global and local state variables defined in Section 2.6, the derivatives needed for sensitivity analysis (Eq. (23)) are presented in this appendix. In the expressions below, use is made of the products $\boxtimes$ and $\boxdot$ between two second order tensors, defined in Appendix A as $(\boldsymbol{A}\boxtimes\boldsymbol{B})_{ijkl} = A_{ik}B_{jl}$ and $(\boldsymbol{A}\boxtimes\boldsymbol{B})_{ijkl} = A_{il}B_{jk}$.

B.1: Derivatives of global constraints

The derivative of the global constraint $\boldsymbol{R}^k$ with respect to the element density variable vector $\boldsymbol{\rho}$ is

$$\frac{\partial\boldsymbol{R}^k}{\partial\boldsymbol{\rho}} = \begin{bmatrix} \overset{n_{ele}}{\underset{e=1}{\mathcal{A}}}\left(\frac{\partial\boldsymbol{F}^{e^k}_{int}}{\partial\rho_e}\right) \\ \boldsymbol{0} \end{bmatrix} \tag{B.1}$$

with

$$\begin{aligned} \frac{\partial\boldsymbol{F}^{e^k}_{int}}{\partial\rho_e} &= \sum_{r=1}^{n_{ipt}} w_r r_{e_r}^{k^{a-1}}\boldsymbol{B}^T_{e_r}\frac{\partial\widetilde{\boldsymbol{P}}^k_{e_r}}{\partial\rho_e} \\ \frac{\partial\widetilde{\boldsymbol{P}}^k_{e_r}}{\partial\rho_e} &= \frac{\partial\chi_H}{\partial\rho_e}\widetilde{\boldsymbol{\tau}}^{VP^k}_{e_r}.\widetilde{\mathbf{F}}^{k^{-T}}_{e_r} + \frac{\partial\chi_S}{\partial\rho_e}\widetilde{\boldsymbol{P}}^{HE^k}_{e_r} \end{aligned} \tag{B.2}$$

The derivatives with respect to the global variables $\hat{\boldsymbol{u}}$ are

$$\frac{\partial\boldsymbol{R}^k}{\partial\hat{\boldsymbol{u}}^{k-1}} = \boldsymbol{0}; \;\; \frac{\partial\boldsymbol{R}^k}{\partial\hat{\boldsymbol{u}}^k} = \begin{bmatrix} \overset{n_{ele}}{\underset{e=1}{\mathcal{A}}}\left(\frac{\partial\boldsymbol{F}^{e^k}_{int}}{\partial\boldsymbol{u}^k_e}\right) & \boldsymbol{A}^T \\ \boldsymbol{A} & \boldsymbol{0} \end{bmatrix} \tag{B.3}$$

and the term $\partial\boldsymbol{F}^{e^k}_{int}/\,\partial\boldsymbol{u}^k_e$ is given as

$$\begin{aligned} \frac{\partial\boldsymbol{F}^{e^k}_{int}}{\partial\boldsymbol{u}^k_e} &= \sum_{r=1}^{n_{ipt}} w_r r_{e_r}^{k^{a-1}}\boldsymbol{B}^T_{e_r}\frac{\partial\widetilde{\boldsymbol{P}}^k_{e_r}}{\partial\boldsymbol{u}^k_e} + (a-1)\sum_{r=1}^{n_{ipt}} w_r r_{e_r}^{k^{a-2}}\boldsymbol{B}^T_{e_r}\widetilde{\boldsymbol{P}}^k_{e_r}\otimes\frac{\partial r^k_{e_r}}{\partial\boldsymbol{u}^k_e} \\ \frac{\partial\widetilde{\boldsymbol{P}}^k_{e_r}}{\partial\boldsymbol{u}^k_e} &= \left(\chi_S\widetilde{\mathbb{A}}^{HE^k}_{e_r} - \chi_H\widetilde{\boldsymbol{P}}^{VP^k}_{e_r}\boxdot\widetilde{\boldsymbol{F}}^{k^{-1}}_{e_r}\right) : \frac{\partial\widetilde{\boldsymbol{F}}^k_{e_r}}{\partial\boldsymbol{u}^k_e} \\ \frac{\partial r^k_{e_r}}{\partial\boldsymbol{u}^k_{\boldsymbol{e}}} &= r^k_{e_r}\left(\boldsymbol{F}^{k^{-T}}_{0_{\boldsymbol{e_r}}} : \frac{\partial\boldsymbol{F}^k_{0_{e_r}}}{\partial u^k_e} - \boldsymbol{F}^{k^{-T}}_{e_r} : \frac{\partial\boldsymbol{F}^k_{e_r}}{\partial\boldsymbol{u}^k_e}\right) \end{aligned} \tag{B.4}$$

Finally, the derivatives with respect to the local variables $\boldsymbol{c}$ are

$$\frac{\partial\boldsymbol{R}^k}{\partial\boldsymbol{c}^{k-1}} = \boldsymbol{0}; \;\; \frac{\partial\boldsymbol{R}^k}{\partial\boldsymbol{c}^k} = \begin{bmatrix} \overset{n_{ele}}{\underset{e=1}{\mathcal{A}}}\left(\frac{\partial\boldsymbol{F}^{e^k}_{int}}{\partial\boldsymbol{c}^k_e}\right) \\ \boldsymbol{0} \end{bmatrix} \tag{B.5}$$

with

$$\frac{\partial\boldsymbol{F}^{e^k}_{int}}{\partial\boldsymbol{c}^k_e} = \begin{bmatrix} \frac{\partial\boldsymbol{F}^{e^k}_{int}}{\partial\boldsymbol{c}^k_{e_1}} & \frac{\partial\boldsymbol{F}^{e^k}_{int}}{\partial\boldsymbol{c}^k_{e_2}} & \frac{\partial\boldsymbol{F}^{e^k}_{int}}{\partial\boldsymbol{c}^k_{e_3}} & \frac{\partial\boldsymbol{F}^{e^k}_{int}}{\partial\boldsymbol{c}^k_{e_4}} \end{bmatrix} \tag{B.6}$$

The derivatives $\partial\boldsymbol{F}^{e^k}_{int}/\partial\boldsymbol{c}^k_{e_r}$ are

$$\frac{\partial\boldsymbol{F}^{e^k}_{int}}{\partial\boldsymbol{c}^k_{e_r}} = \begin{bmatrix} w_r r_{e_r}^{k^{a-1}}\boldsymbol{B}^T_{e_r}\frac{\partial\widetilde{\boldsymbol{P}}^k_{e_r}}{\partial\boldsymbol{b}^{e^k}_{e_r}} & \boldsymbol{0} & \boldsymbol{0} \end{bmatrix}^T$$

and

$$\frac{\partial\widetilde{\boldsymbol{P}}^k_{e_r}}{\partial\boldsymbol{b}^{e^k}_{e_r}} = \frac{\partial\left(\chi_H\widetilde{\boldsymbol{\tau}}^{VP^k}_{e_r}.\widetilde{\mathbf{F}}^{k^{-T}}_{e_r}\right)}{\partial\boldsymbol{b}^{e^k}_{e_r}} \tag{B.7}$$

In Eq. (B.7), the term $\partial\bar{\boldsymbol{P}}^k_{e_r}/\partial\boldsymbol{b}^{e^k}_{e_r}$ has the component form

$$\frac{\partial\tau_{ip}F^{-T}_{pj}}{\partial b^e_{kl}} = \frac{\partial\tau_{ip}}{\partial b^e_{kl}}F^{-T}_{pj} \tag{B.8}$$

and $\partial\bar{\boldsymbol{\tau}}^{VP}/\partial\boldsymbol{b}^e$ can be computed in the constitutive algorithm.

B.2: Derivatives of local constraints

The derivative of the local constraints $\boldsymbol{H}^k$ with respect to the element density variable vector $\boldsymbol{\rho}$ is given by the block diagonal matrix

$$\frac{\partial \boldsymbol{H}^k}{\partial \boldsymbol{\rho}} = \begin{bmatrix} \frac{\partial \boldsymbol{H}_1^k}{\partial \rho_1} & \mathbf{0} & \dots & \mathbf{0} \\ \mathbf{0} & \frac{\partial \boldsymbol{H}_2^k}{\partial \rho_2} & \dots & \mathbf{0} \\ \vdots & \vdots & \ddots & \vdots \\ \mathbf{0} & \mathbf{0} & \dots & \frac{\partial \boldsymbol{H}_{n_{ele}}^k}{\partial \rho_{n_{ele}}} \end{bmatrix} \quad \text{with} \quad \frac{\partial \boldsymbol{H}_e^k}{\partial \rho_e} = \begin{bmatrix} \frac{\partial \boldsymbol{H}_{e_1}^k}{\partial \rho_e} \\ \frac{\partial \boldsymbol{H}_{e_2}^k}{\partial \rho_e} \\ \frac{\partial \boldsymbol{H}_{e_3}^k}{\partial \rho_e} \\ \frac{\partial \boldsymbol{H}_{e_4}^k}{\partial \rho_e} \end{bmatrix} \tag{B.9}$$

and the entries $\partial \boldsymbol{H}_{e_r}^k / \partial \rho_e$ are only nonzero at a viscoplastic step, having the form

$$\begin{aligned} \frac{\partial \boldsymbol{H}_{e_r}^k}{\partial \rho_e} &= \begin{bmatrix} \frac{\partial \boldsymbol{h}_{e_{r1}}^k}{\partial \rho_e} & 0 & \frac{\partial h_{e_{r3}}^k}{\partial \rho_e} \end{bmatrix}^T \\ \frac{\partial \boldsymbol{h}_{e_{r1}}^k}{\partial \rho_e} &= -\boldsymbol{b}_{e_r}^{e,tr} . \frac{\partial \exp\left[-2\Delta t \boldsymbol{A}_{e_r}^k\right]}{\partial \rho_e} \\ \frac{\partial h_{e_{r3}}^k}{\partial \rho_e} &= \sqrt{\frac{3}{2}} \left(\frac{\Delta t}{\mu \Delta \gamma_{e_r}^k + \Delta t} \right)^{\vartheta} \boldsymbol{n}_{e_r}^k : \left(\frac{\partial \chi_H}{\partial \rho_e} \boldsymbol{\tau}_{e_r}^{VP^k} \right) \end{aligned} \tag{B.10}$$

The term $\partial \exp[-2\Delta t \boldsymbol{A}_{e_r}^k] / \partial \rho_e$ is computed in the principal space, where for each principal value the derivative is

$$\begin{aligned} &\frac{\partial \exp\left[-2\Delta\gamma \sqrt{\frac{3}{2}} n_a\right]}{\partial \rho_e} \\ &= -2\Delta\gamma \sqrt{\frac{3}{2}} \exp\left[-2\Delta\gamma \sqrt{\frac{3}{2}} n_a\right] \frac{\partial n_a}{\partial \tau_a} \left(\frac{\partial \chi_H}{\partial \rho_e} \tau_a \right), \quad a = 1, 2, 3 \end{aligned} \tag{B.11}$$

The derivatives with respect to the global variables $\hat{\boldsymbol{u}}$ are

$$\frac{\partial \boldsymbol{H}^k}{\partial \hat{\boldsymbol{u}}^k} = \begin{bmatrix} \frac{\partial \boldsymbol{H}^k}{\partial \boldsymbol{u}^k} \\ \mathbf{0} \end{bmatrix} \quad \text{and} \quad \frac{\partial \boldsymbol{H}^k}{\partial \hat{\boldsymbol{u}}^{k-1}} = \begin{bmatrix} \frac{\partial \boldsymbol{H}^k}{\partial \boldsymbol{u}^{k-1}} \\ \mathbf{0} \end{bmatrix} \tag{B.12}$$

and the nonzero submatrix $\partial \boldsymbol{H}^k / \partial \boldsymbol{u}^k$ has the structure

$$\frac{\partial \boldsymbol{H}^k}{\partial \boldsymbol{u}^k} = \begin{bmatrix} \frac{\partial \boldsymbol{H}_1^k}{\partial \boldsymbol{u}^k} \\ \vdots \\ \frac{\partial \boldsymbol{H}_{n_{ele}}^k}{\partial \boldsymbol{u}^k} \end{bmatrix} \quad \text{with} \quad \frac{\partial \boldsymbol{H}_j^k}{\partial \boldsymbol{u}^k} = \overset{n_{ele}}{\underset{e=1}{\mathcal{A}}} \left(\frac{\partial \boldsymbol{H}_j^k}{\partial \boldsymbol{u}_e^k} \right), \quad j = 1, 2, \dots, n_{ele} \tag{B.13}$$

Here, $\partial \boldsymbol{H}_j^k / \partial \boldsymbol{u}_e^k = \mathbf{0}$ if $j \neq e$. The nonzero entries, $\partial \boldsymbol{H}_e^k / \partial \boldsymbol{u}_e^k$, are

$$\frac{\partial \boldsymbol{H}_e^k}{\partial \boldsymbol{u}_e^k} = \begin{bmatrix} \frac{\partial \boldsymbol{H}_{e_1}^k}{\partial \boldsymbol{u}_e^k} & \frac{\partial \boldsymbol{H}_{e_2}^k}{\partial \boldsymbol{u}_e^k} & \frac{\partial \boldsymbol{H}_{e_3}^k}{\partial \boldsymbol{u}_e^k} & \frac{\partial \boldsymbol{H}_{e_4}^k}{\partial \boldsymbol{u}_e^k} \end{bmatrix}^T \tag{B.14}$$

with

$$\begin{aligned} \frac{\partial \boldsymbol{H}_{e_r}^k}{\partial \boldsymbol{u}_e^k} &= \begin{bmatrix} -\frac{\partial \boldsymbol{b}_{e_r}^{e,tr}}{\partial \boldsymbol{u}_e^k} & 0 & 0 \end{bmatrix}^T \\ \frac{\partial \boldsymbol{b}_{e_r}^{e,tr}}{\partial \boldsymbol{u}_e^k} &= \frac{\partial \boldsymbol{b}_{e_r}^{e,tr}}{\partial \widetilde{\boldsymbol{F}}_{e_r}^k} : \frac{\partial \widetilde{\boldsymbol{F}}_{e_r}^k}{\partial \boldsymbol{u}_e^k} \\ \frac{\partial \boldsymbol{b}_{e_r}^{e,tr}}{\partial \overset{\sim k}{\mathbf{F}}_{e_r}} &= \boldsymbol{I} \boxtimes \boldsymbol{\Delta} \overset{\sim k}{\mathbf{F}}_{e_r} . \boldsymbol{b}_{e_r}^{e^{k-1^T}} . \widetilde{\boldsymbol{F}}_{e_r}^{k-1^{-T}} + \boldsymbol{\Delta} \overset{\sim k}{\mathbf{F}}_{e_r} . \boldsymbol{b}_{e_r}^{e^{k-1}} . \overset{\sim k-1^{-T}}{\mathbf{F}}_{e_r} \boxdot \boldsymbol{I} \end{aligned} \tag{B.15}$$

for an elastic step, and

$$\frac{\partial \boldsymbol{H}_{e_r}^k}{\partial \boldsymbol{u}_e^k} = \begin{bmatrix} -\frac{\partial \boldsymbol{b}_{e_r}^{e,tr}}{\partial \boldsymbol{u}_e^k} . \exp\left[-2\Delta t \boldsymbol{A}_{e_r}^k\right] & 0 & 0 \end{bmatrix}^T \tag{B.16}$$

for a plastic step. The nonzero submatrix $\partial \boldsymbol{H}^k / \partial \boldsymbol{u}^{k-1}$ in Eq. (B.12) has the same structure as in Eqns. (B.13) and (B.14), and the nonzero entries $\partial \boldsymbol{H}_{e_r}^k / \partial \boldsymbol{u}_e^{k-1}$ are

$$\begin{aligned} \frac{\partial \boldsymbol{H}_{e_r}^k}{\partial \boldsymbol{u}_e^{k-1}} &= \begin{bmatrix} -\frac{\partial \boldsymbol{b}_{e_r}^{e,tr}}{\partial \boldsymbol{u}_e^{k-1}} & 0 & 0 \end{bmatrix}^T \\ \frac{\partial \boldsymbol{b}_{e_r}^{e,tr}}{\partial \boldsymbol{u}_e^{k-1}} &= \frac{\partial \boldsymbol{b}_{e_r}^{e,tr}}{\partial \widetilde{\boldsymbol{F}}_{e_r}^{k-1}} : \frac{\partial \widetilde{\boldsymbol{F}}_{e_r}^{k-1}}{\partial \boldsymbol{u}_e^{k-1}} \\ \frac{\partial \boldsymbol{b}_{e_r}^{e,tr}}{\partial \overset{\sim k-1}{\mathbf{F}}_{e_r}} &= -\boldsymbol{\Delta} \overset{\sim k}{\boldsymbol{F}}_{e_r} \boxtimes \boldsymbol{\Delta} \overset{\sim k}{\mathbf{F}}_{e_r} . b_{e_r}^{e^{k-1^T}} . \overset{\sim k-1^{-T}}{\mathbf{F}}_{e_r} \\ &\quad - \boldsymbol{\Delta} \overset{\sim k}{\mathbf{F}}_{e_r} . \boldsymbol{b}_{e_r}^{e^{k-1}} . \overset{\sim k-1^{-T}}{\mathbf{F}}_{e_r} \boxdot \boldsymbol{\Delta} \tilde{F}_{e_r}^k \end{aligned} \tag{B.17}$$

for an elastic step and

$$\frac{\partial \boldsymbol{H}_{e_r}^k}{\partial \boldsymbol{u}_e^{k-1}} = \begin{bmatrix} -\frac{\partial \boldsymbol{b}_{e_r}^{e,tr}}{\partial \boldsymbol{u}_e^{k-1}} . \exp\left[-2\Delta t \boldsymbol{A}_{e_r}^k\right] & 0 & 0 \end{bmatrix}^T \tag{B.18}$$

for a plastic step.

The nonzero derivatives $\partial \boldsymbol{H}^k / \partial \boldsymbol{c}^k$ and $\partial \boldsymbol{H}^k / \partial \boldsymbol{c}^{k-1}$, have the block diagonal matrix form

$$\begin{aligned} \frac{\partial \boldsymbol{H}^k}{\partial \boldsymbol{c}^k} &= \begin{bmatrix} \frac{\partial \boldsymbol{H}_1^k}{\partial \boldsymbol{c}_1^k} & \mathbf{0} & \dots & \mathbf{0} \\ \mathbf{0} & \frac{\partial \boldsymbol{H}_2^k}{\partial \boldsymbol{c}_2^k} & \dots & \mathbf{0} \\ \vdots & \vdots & \ddots & \vdots \\ \mathbf{0} & \mathbf{0} & \dots & \frac{\partial \boldsymbol{H}_{n_{ele}}^k}{\partial \boldsymbol{c}_{n_{ele}}^k} \end{bmatrix}, \\ \frac{\partial \boldsymbol{H}^k}{\partial \boldsymbol{c}^{k-1}} &= \begin{bmatrix} \frac{\partial \boldsymbol{H}_1^k}{\partial \boldsymbol{c}_1^{k-1}} & \mathbf{0} & \dots & \mathbf{0} \\ \mathbf{0} & \frac{\partial \boldsymbol{H}_2^k}{\partial \boldsymbol{c}_2^{k-1}} & \dots & \mathbf{0} \\ \vdots & \vdots & \ddots & \vdots \\ \mathbf{0} & \mathbf{0} & \dots & \frac{\partial \boldsymbol{H}_{n_{ele}}^k}{\partial \boldsymbol{c}_{n_{ele}}^{k-1}} \end{bmatrix} \end{aligned} \tag{B.19}$$

due to the fact that $\boldsymbol{c}_e^k$ and $\boldsymbol{c}_j^k$ are independent of each other and that $\boldsymbol{H}_e^k$ and $\boldsymbol{H}_j^k$ are uncoupled for $j \neq e$. The submatrices $\partial \boldsymbol{H}_e^k / \partial \boldsymbol{c}_e^k$

have this structure for the same reasons, i.e.

$$\frac{\partial \boldsymbol{H}_e^k}{\partial \boldsymbol{c}_e^k} = \begin{bmatrix} \frac{\partial \boldsymbol{H}_{e_1}^k}{\partial \boldsymbol{c}_{e_1}^k} & \mathbf{0} & \mathbf{0} & \mathbf{0} \\ \mathbf{0} & \frac{\partial \boldsymbol{H}_{e_2}^k}{\partial \boldsymbol{c}_{e_2}^k} & \mathbf{0} & \mathbf{0} \\ \mathbf{0} & \mathbf{0} & \frac{\partial \boldsymbol{H}_{e_3}^k}{\partial \boldsymbol{c}_{e_3}^k} & \mathbf{0} \\ \mathbf{0} & \mathbf{0} & \mathbf{0} & \frac{\partial \boldsymbol{H}_{e_4}^k}{\partial \boldsymbol{c}_{e_4}^k} \end{bmatrix},$$

$$\frac{\partial \boldsymbol{H}_e^k}{\partial \boldsymbol{c}_e^{k-1}} = \begin{bmatrix} \frac{\partial \boldsymbol{H}_{e_1}^k}{\partial \boldsymbol{c}_{e_1}^{k-1}} & \mathbf{0} & \mathbf{0} & \mathbf{0} \\ \mathbf{0} & \frac{\partial \boldsymbol{H}_{e_2}^k}{\partial \boldsymbol{c}_{e_2}^{k-1}} & \mathbf{0} & \mathbf{0} \\ \mathbf{0} & \mathbf{0} & \frac{\partial \boldsymbol{H}_{e_3}^k}{\partial \boldsymbol{c}_{e_3}^{k-1}} & \mathbf{0} \\ \mathbf{0} & \mathbf{0} & \mathbf{0} & \frac{\partial \boldsymbol{H}_{e_4}^k}{\partial \boldsymbol{c}_{e_4}^{k-1}} \end{bmatrix} \tag{B.20}$$

The nonzero entries $\partial \boldsymbol{H}_{e_r}^k / \partial \boldsymbol{c}_{e_r}^k$ are

$$\frac{\partial \boldsymbol{H}_{e_r}^k}{\partial \boldsymbol{c}_{e_r}^k} = \begin{bmatrix} \mathbb{I}_4^s & \mathbf{0} & \mathbf{0} \\ \mathbf{0} & 1 & 0 \\ \mathbf{0} & 0 & 1 \end{bmatrix} \tag{B.21}$$

for an elastic step, and

$$\frac{\partial \boldsymbol{H}_{e_r}^k}{\partial \boldsymbol{c}_{e_r}^k} = \begin{bmatrix} \mathbb{I}_4^s - \boldsymbol{b}_{e_r}^{e,tr} . \frac{\partial \exp\left[-2\Delta t \boldsymbol{A}_{e_r}^k\right]}{\partial \boldsymbol{b}_{e_r}^{ek}} & \mathbf{0} & -\boldsymbol{b}_{e_r}^{e,tr} . \frac{\partial \exp\left[-2\Delta t \boldsymbol{A}_{e_r}^k\right]}{\Delta \gamma_{e_r}^k} \\ \mathbf{0} & 1 & -1 \\ \sqrt{\frac{3}{2}} \left(\frac{\Delta t}{\mu \Delta \gamma_{e_r}^k + \Delta t} \right)^{\vartheta} \boldsymbol{n}_{e_r}^k : \frac{\partial \boldsymbol{\tau}_{e_r}^{VPk}}{\partial \boldsymbol{b}_{e_r}^{ek}} & -\left. \frac{\partial \zeta}{\partial \alpha} \right|_{\alpha = \alpha_{e_r}^k} & -c_0 \end{bmatrix}$$

$$c_0 = \sqrt{\frac{3}{2}} \left(\frac{\Delta t}{\mu \Delta \gamma_{e_r}^k + \Delta t} \right)^{\vartheta} \frac{\vartheta \mu || \boldsymbol{s}_{e_r}^{VPk} ||}{\mu \Delta \gamma_{e_r}^k + \Delta t} \tag{B.22}$$

for a plastic step. Again, the derivatives of the term $\exp[-2\Delta t \boldsymbol{A}_{e_r}^k]$ are computed in the principal space as

$$\frac{\partial \exp\left[-2\Delta\gamma \sqrt{\frac{3}{2}} n_a\right]}{\partial b_b^e} = -2\Delta\gamma \sqrt{\frac{3}{2}} \exp\left[-2\Delta\gamma \sqrt{\frac{3}{2}} n_a\right] \times \frac{\partial n_a}{\partial \tau_c} \left(\chi_H \frac{\partial \tau_c}{\partial b_b^e} \right), \quad a, b, c = 1, 2, 3$$

$$\frac{\partial \exp\left[-2\Delta\gamma \sqrt{\frac{3}{2}} n_a\right]}{\partial \Delta\gamma} = -2\sqrt{\frac{3}{2}} \exp\left[-2\Delta\gamma \sqrt{\frac{3}{2}} n_a\right] n_a \tag{B.23}$$

Finally, the nonzero entries of the derivative matrix $\partial \boldsymbol{H}^k / \partial \boldsymbol{c}^{k-1}$ are

$$\frac{\partial \boldsymbol{H}_{e_r}^k}{\partial \boldsymbol{c}_{e_r}^{k-1}} = \begin{bmatrix} -\frac{\partial \boldsymbol{b}_{e_r}^{e,tr}}{\partial \boldsymbol{b}_{e_r}^{ek-1}} & \mathbf{0} & \mathbf{0} \\ \mathbf{0} & -1 & 0 \\ \mathbf{0} & 0 & 0 \end{bmatrix}$$

$$\frac{\partial \boldsymbol{b}_{e_r}^{e,tr}}{\partial \boldsymbol{b}_{e_r}^{ek-1}} = \frac{1}{2} \left(\Delta \overset{\sim}{\mathbf{F}}{}_{e_r}^{k} \boxtimes \Delta \overset{\sim}{\mathbf{F}}{}_{e_r}^{k} + \boldsymbol{\Delta} \tilde{F}_{e_r}^k \boxdot \boldsymbol{\Delta} \tilde{F}_{e_r}^k \right) \tag{B.24}$$

for an elastic step and

$$\frac{\partial \boldsymbol{H}_{e_r}^k}{\partial \boldsymbol{c}_{e_r}^{k-1}} = \begin{bmatrix} -\frac{\partial \boldsymbol{b}_{e_r}^{e,tr}}{\partial \boldsymbol{b}_{e_r}^{ek-1}} . \exp\left[-2\Delta t \boldsymbol{A}_{e_r}^k\right] & \mathbf{0} & \mathbf{0} \\ \mathbf{0} & -1 & 0 \\ \mathbf{0} & 0 & 0 \end{bmatrix} \tag{B.25}$$

where $\frac{\partial b_{ip}^{e,tr} \exp[-2\Delta t A_{pj}]}{\partial b_{kl}^{e,k-1}} = \frac{\partial b_{ip}^{e,tr}}{\partial b_{kl}^{e,k-1}} \exp[-2\Delta t A_{pj}]$ for a plastic step.

B.3: Derivatives of objective function

Discretizing the plastic work used to evaluate the objective function (Eq. (20)) using the trapezoid rule gives

$$W^p \approx \sum_{k=1}^{n} \left(\sum_{e=1}^{n_{ele}} \left(\sum_{r=1}^{n_{ipt}} \left(w_r \chi_A \sqrt{\frac{3}{2}} \Delta \gamma_{e_r}^k \boldsymbol{\tau}_{e_r}^{VP^k} : \boldsymbol{n}_{e_r}^k \right) \right) \right) \tag{B.26}$$

From this, it can be seen that the nonzero derivatives are $\partial W^p / \partial \boldsymbol{\rho}$ and $\partial W^p / \partial \boldsymbol{c}^k$, which are given as

$$\frac{\partial W^p}{\partial \boldsymbol{\rho}} = \begin{bmatrix} \frac{\partial W^p}{\partial \rho_1} & \frac{\partial W^p}{\partial \rho_2} & \cdots & \frac{\partial W^p}{\partial \rho_{n_{ele}}} \end{bmatrix}$$

$$\frac{\partial W^p}{\partial \rho_e} = \sum_{k=1}^{n} \left(\sum_{r=1}^{n_{ipt}} \left(\frac{\partial \chi_A}{\partial \rho_e} w_r \sqrt{\frac{3}{2}} \Delta \gamma_{e_r}^k \boldsymbol{\tau}_{e_r}^{VP^k} : \boldsymbol{n}_{e_r}^k + \chi_A w_r \sqrt{\frac{3}{2}} \Delta \gamma_{e_r}^k \frac{\partial \boldsymbol{\tau}_{e_r}^{VP^k}}{\partial \rho_e} : \boldsymbol{n}_{e_r}^k \right) \right)$$

$$\frac{\partial \boldsymbol{\tau}_{e_r}^{VP^k}}{\partial \rho_e} = \frac{\partial \chi_H}{\partial \rho_e} \left(2 \frac{\partial \psi_{VP}}{\partial \boldsymbol{b}^e} . \boldsymbol{b}^e \right) \tag{B.27}$$

and

$$\frac{\partial W^p}{\partial \boldsymbol{c}^k} = \begin{bmatrix} \frac{\partial W^p}{\partial \boldsymbol{c}_1^k} & \frac{\partial W^p}{\partial \boldsymbol{c}_2^k} & \cdots & \frac{\partial W^p}{\partial \boldsymbol{c}_{n_{ele}}^k} \end{bmatrix}$$

$$\frac{\partial W^p}{\partial \boldsymbol{c}_e^k} = \begin{bmatrix} \frac{\partial W^p}{\partial \boldsymbol{c}_{e_1}^k} & \frac{\partial W^p}{\partial \boldsymbol{c}_{e_2}^k} & \frac{\partial W^p}{\partial \boldsymbol{c}_{e_3}^k} & \frac{\partial W^p}{\partial \boldsymbol{c}_{e_4}^k} \end{bmatrix}$$

$$\frac{\partial W^p}{\partial \boldsymbol{c}_{e_r}^k} = \chi_A w_r \sqrt{\frac{3}{2}} \begin{bmatrix} \Delta \gamma_{e_r}^k \left(\frac{\partial \boldsymbol{\tau}_{e_r}^{VP^k}}{\partial \boldsymbol{b}_{e_r}^{ek}} : \boldsymbol{n}_{e_r}^k + \boldsymbol{\tau}_{\boldsymbol{e_r}}^{VP^k} : \frac{\partial \boldsymbol{n}_{e_r}^k}{\partial \boldsymbol{b}_{e_r}^{ek}} \right) & 0 & \boldsymbol{\tau}_{e_r}^{VP^k} : \boldsymbol{n}_{e_r}^k \end{bmatrix}^{\boldsymbol{T}} \tag{B.28}$$

where the derivatives $\partial \boldsymbol{\tau}_{e_r}^{VP^k} / \partial \boldsymbol{b}_{e_r}^{ek}$ and $\partial \boldsymbol{n}_{e_r}^k / \partial \boldsymbol{b}_{e_r}^{ek}$ are evaluated in principal space and then transformed to physical space.

Appendix C. Verification of sensitivity analysis

In this Appendix, implementation of the adjoint sensitivity analysis is verified by comparing the values obtained using the adjoint method to those obtained using the central difference method

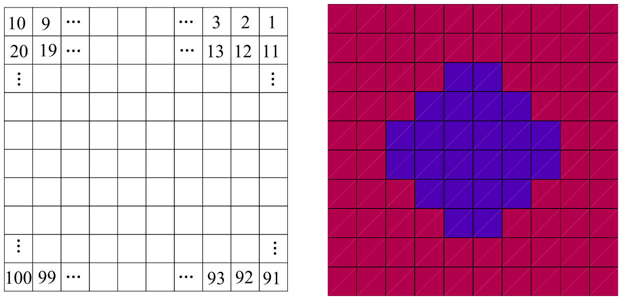

a) Element numbering b) Density distribution

Fig. C.1. Square RUC domain for sensitivity verification with element numbering and density distribution.

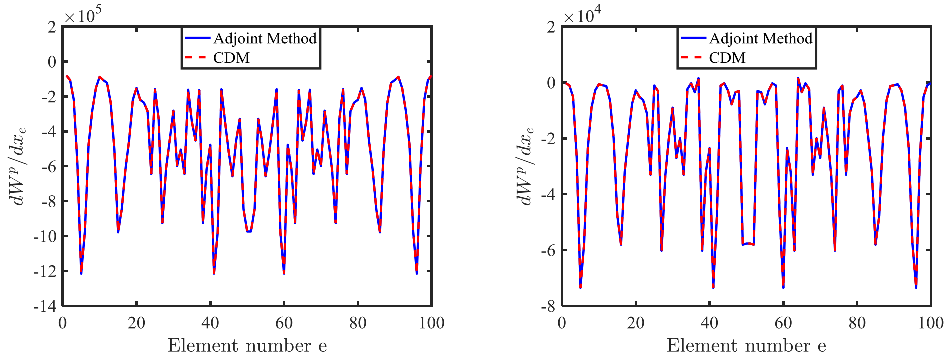

a) No Rate Effects

b) Rate Effects: $\mu/t_n = 500$

Fig. C.2. Comparison of sensitivity values obtained using the adjoint method and CDM with $\Delta h = 10^{-5}$ for two cases of rate effects in elasto-viscoplastic glassy polymer phase under simple shear.

(CDM). The sensitivity of the total plastic work W^P with respect to design variable x_e is calculated using the CDM as follows

$$\frac{dW^P(\boldsymbol{x})}{dx_e} \approx \frac{W^P(\boldsymbol{x}+\Delta\boldsymbol{h}) - W^P(\boldsymbol{x}-\Delta\boldsymbol{h})}{2\Delta\boldsymbol{h}} \tag{C.1}$$

where $\Delta\boldsymbol{h}$ is a vector containing all zeros except at the component corresponding to x_e, which has the perturbation value Δh, here taken as 10^{-5}. The example used for sensitivity verification is a square RUC domain of dimensions 1000 by 1000 discretized into a 10 × 10 mesh of plane strain F-bar elements with a thickness of 1. The density distribution is set to correspond to that discussed in Section 2.5, i.e. a matrix of glassy polymer phase and circular inclusion of soft elastomer phase with the radius set so that the area of the inclusion corresponds to a volume fraction of 0.5. For this example the density values used in the hard glassy polymer matrix are $\rho_H = 0.7$ while the density values used in the soft elastomer inclusion are $\rho_S = 0.3$. Fig. C.1a shows the discretized domain and element numbering while Fig. C.1b shows the initial density distribution. The material parameters discussed in Section 2.4 are utilized and no filter is considered (i.e. $dW^P/\partial\boldsymbol{x} = dW^P/\partial\boldsymbol{\rho}$).

This RUC is subject to a simple shear deformation mode under 30% strain ($\nabla\hat{\boldsymbol{u}} = [0 \quad 0.3 \quad 0.3 \quad 0]$) for two cases. In the first case no rate effects are considered in the elasto-viscoplastic glassy polymer phase (i.e. $\vartheta = 0$ in the viscoplastic model) while the second case considers rate effects using $\vartheta = 1$ and a ratio between the viscosity parameter and total deformation time $\mu/t_n = 500$, corresponding to a high rate of deformation. The sensitivity values obtained using the adjoint method and CDM for both cases are shown in Fig. C.2, where it can be seen that the sensitivity values match closely, verifying the correct implementation of the path-dependent adjoint sensitivity analysis.

References

Al-Ketan, O., Adel Assad, M., Abu Al-Rub, R.K., 2017. Mechanical properties of periodic interpenetrating phase composites with novel architected microstructures. Compos. Struct. 176, 9–19.

Alberdi, R., Khandelwal, K., 2019a. Bi-material topology optimization for energy dissipation with inertia and material rate effects under finite deformations. Finite Elem. Anal. Des. 164, 18–41.

Alberdi, R., Khandelwal, K., 2019b. Design of periodic elastoplastic energy dissipating microstructures. Struct. Multidiscip. Optim. 59, 461–483.

Alberdi, R., Zhang, G., Khandelwal, K., 2018a. A framework for implementation of RVE-based multiscale models in computational homogenization using isogeometric analysis. Int. J. Numer. Methods Eng. 114, 1018–1051.

Alberdi, R., Zhang, G., Li, L., Khandelwal, K., 2018b. A unified framework for nonlinear path-dependent sensitivity analysis in topology optimization. Int. J. Numer. Methods Eng. 115, 1–56.

Amstutz, S., Giusti, S.M., Novotny, A.A., de Souza Neto, E.A., 2010. Topological derivative for multi-scale linear elasticity models applied to the synthesis of microstructures. Int. J. Numer. Methods Eng. 84, 733–756.

Andreasen, C.S., Andreassen, E., Jensen, J.S., Sigmund, O., 2014. On the realization of the bulk modulus bounds for two-phase viscoelastic composites. J. Mech. Phys. Solids 63, 228–241.

Armero, F., 2017. Elastoplastic and viscoplastic deformations in solids and structures. In: Stein, E., De Borst, R., Hughes, T.J.R. (Eds.), Encyclopedia of Computational Mechanics. John Wiley & Sons, Ltd., pp. 227–266.

Barthelat, F., 2015. Architectured materials in engineering and biology: fabrication, structure, mechanics and performance. Int. Mater. Rev. 60, 413–430.

Bendsøe, M.P., Sigmund, O., 2003. Topology Optimization: Theory, Methods and Applications. Springer, Berlin.

Bendsøe, P.M., Sigmund, O., 1999. Material interpolation schemes in topology optimization. Arch. Appl. Mech. 69, 635–654.

Blanco, P.J., Sanchez, P.J., de Souza Neto, E.A., Feijoo, R.A., 2016. Variational foundations and generalized unified theory of RVE-Based multiscale models. Arch. Comput. Meth. Eng. 23, 191–253.

Bortot, E., Amir, O., Shmuel, G., 2018. Topology optimization of dielectric elastomers for wide tunable band gaps. Int. J. Solids Struct. 143, 262–273.

Bourdin, B., 2001. Filters in topology optimization. Int. J. Numer. Methods Eng. 50, 2143–2158.

Bruns, T.E., Tortorelli, D.A., 2001. Topology optimization of non-linear elastic structures and compliant mechanisms. Comput. Methods Appl. Mech. Eng. 190, 3443–3459.

Chen, W., Liu, S., 2014. Topology optimization of microstructures of viscoelastic damping materials for a prescribed shear modulus. Struct. Multidiscip. Optim. 50, 287–296.

Chen, Y., Wang, L., 2014. Periodic co-continuous acoustic metamaterials with overlapping locally resonant and Bragg band gaps. Appl. Phys. Lett. 105, 191907.

Cho, H., Weaver, J.C., Poselt, E., in't Veld, P.J., Boyce, M.C., Rutledge, G.C., 2016. Engineering the mechanics of heterogeneous soft crystals. Adv. Funct. Mater. 26, 6938–6949.

Clausen, A., Wang, F., Jensen, J.S., Sigmund, O., Lewis, J.A., 2015. Topology optimized architectures with programmable poisson's ratio over large deformations. Adv. Mater. 27, 5523–5527.

Crisfield, M.A., 1991. Non-linear Finite Element Analysis of Solids and Structures. John Wiley & Sons Ltd, West Sussex, England.

David, N.V., Gao, X.L., Zheng, J.Q., 2009. Ballistic resistant body armor: contemporary and prospective materials and related protection mechanisms. Appl. Mech. Rev. 62 050802-050802-050820.

de Souza Neto, E.A., Amstutz, S., Giusti, S.M., Novotny, A.A., 2010. Topological derivative-based optimization of micro-structures considering different multi-scale models. CMES 62, 23–56.

de Souza Neto, E.A., Peric, D., Dutko, M., Owen, D.R.J., 1996. Design of simple low order finite elements for large strain analysis of nearly incompressible solids. Int. J. Solids Struct. 33, 3277–3296.

de Souza Neto, E.A., Peric, D., Owen, D.R.J., 2011. Computational Methods For Plasticity: Theory and Applications. John Wiley & Sons Ltd., West Sussex, England.

Firooz, S., Javili, A., 2019. Understanding the role of general interfaces in the overall behavior of composites and size effects. Comput. Mater. Sci. 162, 245–254.

Gibiansky, L.V., Sigmund, O., 2000. Multiphase composites with extremal bulk modulus. J. Mech. Phys. Solids 48, 461–498.

Guest, J.K., Prevost, J.H., 2006. Optimizing multifunctional materials: design of microstructures for maximized stiffness and fluid permeability. Int. J. Solids Struct. 43, 7028–7047.

Hill, R., 1972. On constitutive macro-variables for heterogeneous solids at finite strain. Proc. R. Soc. Lond. A 326, 131–147.

Hogg, P.J., 2006. Composites in Armor. Science 314, 1100–1101.

Holzapfel, G.A., 2000. Nonlinear Solid Mechanics: A Continuum Approach for Engineering. Wiley.

Khoo, Z.X., Teoh, J.E.M., Liu, Y., Chua, C.K., Yang, S., An, J., Leong, K.F., Yeong, W.Y., 2015. 3D printing of smart materials: a review on recent progresses in 4D printing. Virtual Phys. Prototyp. 10, 103–122.

Kook, J., Jensen, J.S., 2017. Topology optimization of periodic microstructures for enhanced loss factor using acousticâ€"structure interaction. Int. J. Solids Struct. 122-123, 59–68.

Landel, R.F., Nielsen, L.E., 1993. Mechanical Properties of Polymers and Composites. CRC press.

Li, L., Khandelwal, K., 2015. Volume preserving projection filters and continuation methods in topology optimization. Eng. Struct. 85, 144–161.

Li, L., Zhang, G., Khandelwal, K., 2018. Failure resistant topology optimization of structures using nonlocal elastoplastic-damage model. Struct. Multidiscip. Optim. 58, 1589–1618.

Mai, Y.-W., Yu, Z.-Z., 2006. Polymer Nanocomposites. Woodhead Publishing.

Mandel, J., 1966. Contribution theorique a l'etude de l'ecrouissage et des lois de l'ecoulement plastique. In: Applied Mechanics. Springer, pp. 502–509.

Neves, M.M., Rodrigues, H., Guedes, J.M., 2000. Optimal design of periodic linear elastic microstructures. Comput. Struct. 76, 421–429.

Perić, D., 1993. On a class of constitutive equations in viscoplasticity: formulation and computational issues. Int. J. Numer. Methods Eng. 36, 1365–1393.

Peric, D., Dettmer, W., 2003. A computational model for generalized inelastic materials at finite strains combining elastic, viscoelastic and plastic material behaviour. Eng. Comput. (Swansea) 20, 768–787.

Sabet, F.A., Su, F.Y., McKittrick, J., Jasiuk, I., 2018. Mechanical properties of model two-phase composites with continuous compared to discontinuous phases. Adv. Eng. Mater. 0.

Saeb, S., Steinmann, P., Javili, A., 2019a. Designing tunable composites with general interfaces. Int. J. Solids Struct. 171, 181–188.

Saeb, S., Steinmann, P., Javili, A., 2019b. On effective behavior of microstructures embedding general interfaces with damage. Comput. Mech. 64, 1473–1494.

Sigmund, O., 2000. A new class of extremal composites. J. Mech. Phys. Solids 48, 397–428.

Svanberg, K., 1987. The method of moving asymptotes—a new method for structural optimization. Int. J. Numer. Methods Eng. 24, 359–373.

Swan, C.C., Arora, J.S., 1997. Topology design of material layout in structured composites of high stiffness and strength. Struct. Optim. 13, 45–59.

Swan, C.C., Kosaka, I., 1997. Homogenization-based analysis and design of composites. Comput. Struct. 64, 603–621.

Vaezi, M., Chianrabutra, S., Mellor, B., Yang, S., 2013. Multiple material additive manufacturing - Part 1: a review. Virtual Phys. Prototyp. 8, 19–50.

Wang, F., Sigmund, O., Jensen, J.S., 2014. Design of materials with prescribed nonlinear properties. J. Mech. Phys. Solids 69, 156–174.

Wang, L., Lau, J., Thomas, E.L., Boyce, M.C., 2011. Co-Continuous composite materials for stiffness, strength, and energy dissipation. Adv. Mater. 23, 1524–1529.

Yi, Y.-M., Park, S.-H., Youn, S.-K., 2000. Design of microstructures of viscoelastic composites for optimal damping characteristics. Int. J. Solids Struct. 37, 4791–4810.

Yun, K.-S., Youn, S.-K., 2018. Microstructural topology optimization of viscoelastic materials of damped structures subjected to dynamic loads. Int. J. Solids Struct. 147, 67–79.

Zhao, N., Wang, Z., Cai, C., Shen, H., Liang, F., Wang, D., Wang, C., Zhu, T., Guo, J., Wang, Y., Liu, X., Duan, C., Wang, H., Mao, Y., Jia, X., Dong, H., Zhang, X., Xu, J., 2014. Bioinspired materials: from low to high dimensional structure. Adv. Mater. 26, 6994–7017.